N73-27173
NASA TN D-7204

NASA TECHNICAL NOTE

NASA TN D-7204

DESIGN AND EVALUATION OF AN OPTICAL FINE-POINTING CONTROL SYSTEM FOR TELESCOPES UTILIZING A DIGITAL STAR SENSOR

by Aaron J. Ostroff and K. C. Romanczyk

Langley Research Center
Hampton, Va. 23665

NATIONAL AERONAUTICS AND SPACE ADMINISTRATION • WASHINGTON, D. C. • JULY 1973

1. Report No.	2. Government Accession No.	3. Recipient's Catalog No.
NASA TN D-7204		

4. Title and Subtitle	5. Report Date
DESIGN AND EVALUATION OF AN OPTICAL FINE-POINTING CONTROL SYSTEM FOR TELESCOPES UTILIZING A DIGITAL STAR SENSOR	July 1973
	6. Performing Organization Code

7. Author(s)	8. Performing Organization Report No.
Aaron J. Ostroff and K. C. Romanczyk	L-8677
	10. Work Unit No.
9. Performing Organization Name and Address	188-78-57-07
NASA Langley Research Center Hampton, Va. 23665	11. Contract or Grant No.
	13. Type of Report and Period Covered
12. Sponsoring Agency Name and Address	Technical Note
National Aeronautics and Space Administration Washington, D.C. 20546	14. Sponsoring Agency Code

15. Supplementary Notes Most of the material presented in this paper is included in a thesis by the first author, entitled "Design of a Star Image Regulating System Utilizing a Digital Sensor," submitted in partial satisfaction of the requirements for the degree of Master of Science, George Washington University, Washington, D.C., February 1971.

16. Abstract

One of the most significant problems associated with the development of large orbiting astronomical telescopes is that of maintaining the very precise pointing accuracy required. A proposed solution to this problem utilizes dual-level pointing control. The primary control system maintains the telescope structure attitude stabilized within a coarse-pointing limit while the fine-pointing system optically stabilizes all star images within the field of view to the desired accuracy. In order to demonstrate the feasibility of optically stabilizing the star images to the desired accuracy a regulating system has been designed and evaluated. The control system utilizes a digital star sensor and an optical star image motion compensator, both of which have been developed for this application. These components have been analyzed mathematically, analytical models have been developed, and hardware has been built and tested.

The system design approach uses a continuous-data network to establish approximate loop gains, break points, and compensation. The objective of the continuous-data analysis, using the familiar s-plane techniques, is to establish a compensatory network that will enable the discrete control system to perform approximately as specified. By using z-transform theory the behavior of the discrete system with this compensation is checked and, if necessary, modifications are made. Next, system dynamic and steady-state performance is tested on an analog computer for the gains and compensation established from the analysis. The simulation includes a measurement of system performance while guiding on a 10th magnitude star. Finally, experimental results, including both static and dynamic checks, are shown for the representative design using actual components.

A discussion and evaluation of an adaptive control technique that is applied to the control loop to improve system accuracy is included.

17. Key Words (Suggested by Author(s))	18. Distribution Statement
Telescope Fine pointing Control	Unclassified – Unlimited

19. Security Classif. (of this report)	20. Security Classif. (of this page)	21. No. of Pages	22. Price*
Unclassified	Unclassified	65	$3.00

*For sale by the National Technical Information Service, Springfield, Virginia 22151

CONTENTS

DESIGN AND EVALUATION OF AN OPTICAL FINE-POINTING CONTROL SYSTEM FOR TELESCOPES UTILIZING A DIGITAL STAR SENSOR*

By Aaron J. Ostroff and K. C. Romanczyk
Langley Research Center

SUMMARY

One of the most significant problems associated with the development of large orbiting astronomical telescopes is that of maintaining the very precise pointing accuracy required. A proposed solution to this problem utilizes dual-level pointing control. The primary control system maintains the telescope structure attitude stabilized within a coarse-pointing limit while the fine-pointing system optically stabilizes all star images within the field of view to the desired accuracy. In order to demonstrate the feasibility of optically stabilizing the star images to the desired accuracy a regulating system has been designed and evaluated. The control system utilizes a digital star sensor and an optical star image motion compensator, both of which have been developed for this application. These components have been analyzed mathematically, analytical models have been developed, and hardware has been built and tested.

The system design approach uses a continuous-data network to establish approximate loop gains, break points, and compensation. The objective of the continuous-data analysis, using the familiar s-plane techniques, is to establish a compensatory network that will enable the discrete control system to perform approximately as specified. By using z-transform theory the behavior of the discrete system with this compensation is checked and, if necessary, modifications are made. Next, system dynamic and steady-state performance is tested on an analog computer for the gains and compensation established from the analysis. The simulation includes a measurement of system performance while guiding on a 10th magnitude star. Finally, experimental results, including both static and dynamic checks, are shown for the representative design using actual components.

A discussion and evaluation of an adaptive control technique that is applied to the control loop to improve system accuracy is included.

---

*Most of the material presented in this paper is included in a thesis by the first author, entitled "Design of a Star Image Regulating System Utilizing a Digital Sensor," submitted in partial satisfaction of the requirements for the degree of Master of Science, George Washington University, Washington, D.C., February 1971.

INTRODUCTION

The relationship of man to the universe has been an intriguing question for many years. Increasingly powerful telescopes, the largest of which is the 5-meter (200-inch) Hale telescope at Mount Palomar, have been constructed for the purpose of studying the planets, the stars, and the universe. Recently, small orbiting telescopes have been developed and flown. An orbiting telescope has the advantage that the collected light does not pass through the earth's atmosphere. The atmosphere absorbs, scatters, or refracts a large part of the incident radiation. The earth's atmosphere is opaque to radiation shorter than 0.3×10^{-6} meter and longer than 30×10^{-6} meter and has many gaps in the transmission range. Even in the transmission range, large ground-based telescopes are limited by scintillation, which causes a sharp stellar image to diffuse and merge with the background.

During the past several years, the National Aeronautics and Space Administration (NASA) has been investigating problems associated with large orbiting astronomical telescopes on the order of 3 meters (120 inches) in diameter. A telescope of 3-meter aperture above the earth's atmosphere would have 10 times the resolving power of the 5-meter telescope on Mount Palomar (refs. 1 and 2). An artist's conception of a 3-meter diffraction-limited telescope attached to a manned space station is shown in figure 1.

Major studies for large orbiting telescopes commenced in the early sixties and included such areas as astronomy, telescope configurations and design, hardware design, active optics, and telescope pointing (refs. 3 to 14). One significant problem is that of maintaining the very precise pointing accuracy required of the telescope. This control must be achieved while guiding on very dim stars – on the order of +10 magnitude – and while the telescope is subjected to environmental and crew motion disturbances.

Several candidate suspension systems, such as a zero-gravity magnetic suspension system, the Apollo Telescope Mount bearing system, and a soft-gimbaled spring suspension system, have been investigated as a means of isolating the telescope from the crew motion disturbances. For any of the suspension systems the range of expected masses and moments of inertia of the telescope indicate that extremely high gains and control torques are required to obtain high-pointing accuracy.

A dual-level control system is one means of alleviating this problem. By using this approach, the telescope structure is controlled within a coarse-pointing limit by the primary attitude control system. A fine-pointing control system, which utilizes small optics internal to the telescope structure, then stabilizes all star images within the field of view to the desired accuracy. This technique allows a significant reduction in the requirement of controlling the entire telescope structure. Furthermore, because of the relatively small inertia of the internal optics, the fine-pointing control system may have

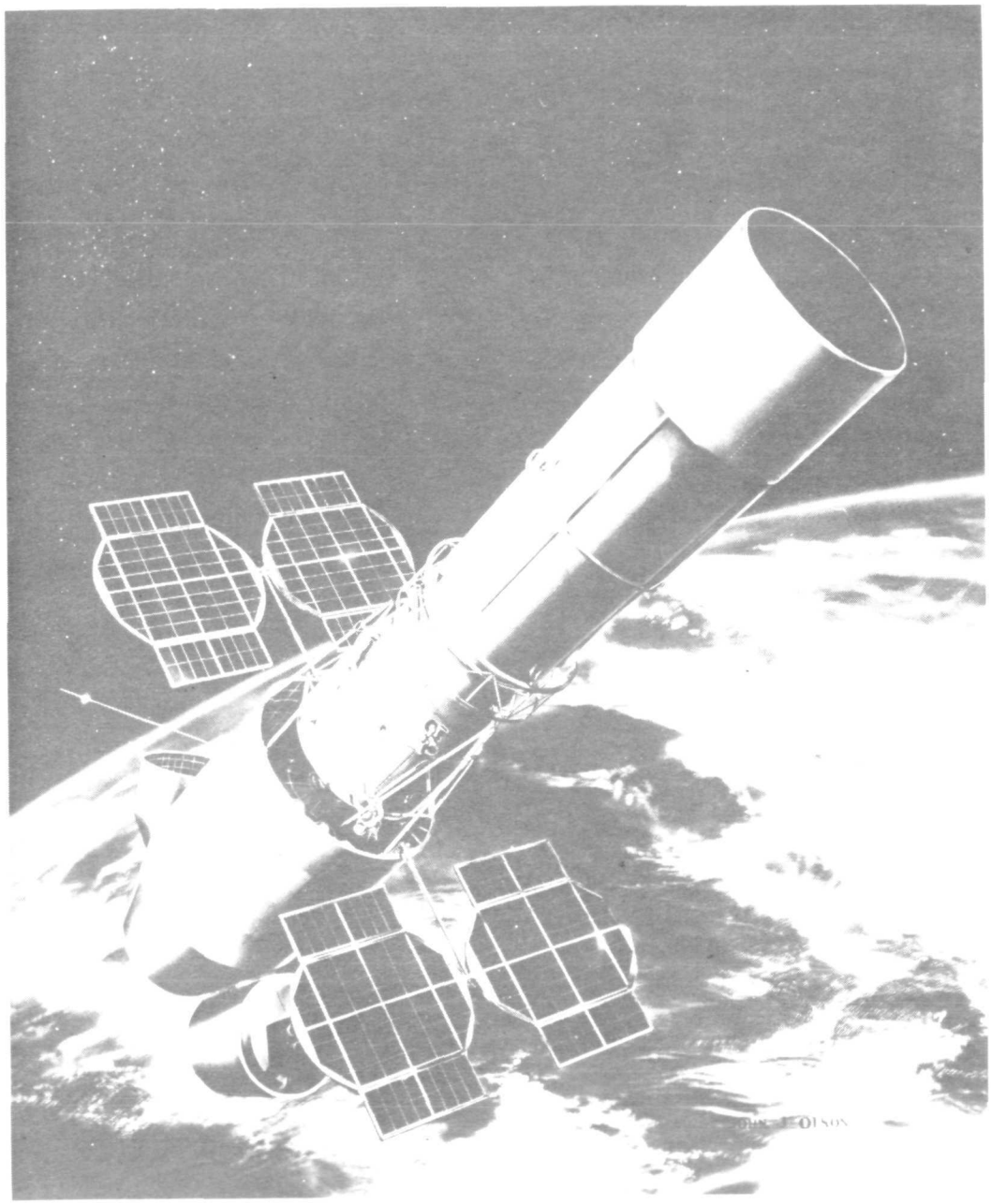

L-70-1570

Figure 1.- Artist's conception of large orbiting telescope attached to manned space station.

a high bandwidth without requiring large control torques and without the likelihood of exciting structural vibrations in the telescope.

The feasibility of operating a fine-pointing control system for a representative telescope within the stability limits of a coarse-pointing control system is demonstrated in this paper. In order to obtain the requisite accuracy and dynamic range, a digital star sensor is included in the design. The section on the star sensor includes a description of the component, the utilization of a mathematical model which is derived in appendix A, and the selection of suitable parameter values with an illustration of a typical example. Star image motion compensation is achieved by utilizing a pair of movable flat mirrors. This paper includes a description of the star image motion compensator and the development of a mathematical model to describe this component. The design approach uses a continuous-data approximation to develop compensation that will make the discrete system perform approximately as specified. The discrete system is evaluated by using z-transform theory, and then dynamic and steady-state performance is analyzed by using an analog computer. Experimental results, including static and dynamic checks, are shown for the representative design using actual hardware. Included in the section on hardware results is a discussion and evaluation of an adaptive control technique that is applied to the control system to improve system accuracy.

SYMBOLS

a	exponential function
B	total equivalent viscous damping, $\frac{\text{newton-meter-seconds}}{\text{radian}}$
b	exponential function
$C_a,\ldots,C_l$	residues
c	exponential function
D_p	viscous damping of image motion compensator, $\frac{\text{newton-meter-seconds}}{\text{radian}}$
E_a	excitation voltage from torque-motor amplifier, volts
E_b	back electromotive force (emf) voltage, volts
E_e	error voltage in rate loop, volts

E_f tachometer feedback voltage, volts

E_h output voltage from zero-order hold, volts

E_r input voltage to rate loop, volts

E_s continuous output voltage from sensor, volts

E_s^* sampled output voltage from sensor, volts

f focal length, meters

G_c transfer function of compensation

G_{ho} transfer function of zero-order hold

G_1 combined transfer function of rate loop and mirror system

G_2 transfer function of sensor

G_3 transfer function of all terms except sensor

I excitation current for torque motor, amperes

i sample number (1, 2, 3, 4)

J_L total load inertia, $\frac{\text{newton-meter-seconds}^2}{\text{radian}}$

J_m inertia of motor, $\frac{\text{newton-meter-seconds}^2}{\text{radian}}$

J_p inertia of image motion compensator, $\frac{\text{newton-meter-seconds}^2}{\text{radian}}$

j complex operator

K general gain constant

K_a gain of torque-motor amplifier, volts/volt

K_b back emf gain constant, $\frac{\text{volt-seconds}}{\text{radian}}$

K_c gain of compensator, volts/volt

K_f gain relating star image displacement to input disturbance, meters/radian

K_m mirror gain constant relating star image displacement to mirror rotation, meters/radian

K_r gain of tachometer, $\frac{\text{volt-seconds}}{\text{radian}}$

K_s gain of sensor, volts/meter-second

K_t torque-motor sensitivity constant, newton-meters/ampere

K_V velocity-error constant, second^{-1}

L torque-motor winding inductance, henrys

m number of terms in expansion

m_d rate of change of star image position on focal plane, meters/second

m_s slope of sweep signal, meters/second

N_1 sensor output number for steady-state case

N_1' sensor output number for velocity input

ΔN_1 error in measured number

n ratio of torque-motor angular rotation to mirror angular rotation

P distance between mirrors when they are both at an angle of 45^o to optic axis, meters

R torque-motor winding resistance, ohms

R_m ratio of sweep signal slope to time rate of change of star image position

$S_o, \ldots, S_5$ dummy variables

s	Laplace operator, $second^{-1}$
T	sampling period, seconds
T_m	torque generated by motor, newton-meters
T_r	restraining torque produced by load, newton-meters
t	time, seconds
t_a	time of first steady-state detection pulse, seconds
t_b	time when steady-state input, velocity input, and sweep signal intersect, seconds
t_c	time when velocity input and sweep signal intersect, seconds
t_d	time of second steady-state detection pulse, seconds
t_1, t_1'	time between first two pulses in train, seconds
t_2, t_2'	time between second two pulses in train, seconds
Δt_a	time interval between first pulse generated by velocity input and first pulse generated by steady-state input, seconds
Δt_b	time interval between second pulse generated by steady-state input and second pulse generated by velocity input, seconds
X_a	peak amplitude of sweep signal, meters
X_b	amplitude of steady-state star image, meters
X_c	amplitude of star moving with constant velocity at time t_c, meters
X_d	star image displacement caused by telescope angular rotation, meters
X_e	star image position on optical focal plane, meters

X_p	star image displacement caused by mirror rotation, meters
X,Y,Z	orthogonal coordinate system
ΔX_b	measured-position error, meters
z	z-transform operator
α	mirror rotation angle, radians
β_c	phase shift of open-loop system, radians
β_m	phase margin, radians
ζ	damping ratio
θ	angular displacement of torque motor, radians
$\dot{\theta}$	angular velocity of torque motor, radians/second
τ	time constant of star sensor model, seconds
ϕ	telescope angular displacement, radians
ϕ_o	magnitude of velocity input disturbance, radians/second
$\dot{\omega}$	radian frequency, radians/second
ω_c	crossover radian frequency, radians/second
ω_d	damped natural frequency, radians/second
ω_s	sampling radian frequency, radians/second
ω_1	numerator break frequency of compensator, radians/second
ω_2	denominator break frequency of compensator, radians/second

ω_3 break frequency of rate loop, radians/second

ω_4 break frequency of star sensor, radians/second

Superscript:

* pulse transfer function

Abbreviation:

Z.O.H. zero-order hold

GENERAL SYSTEM DESCRIPTION

As pointed out in the introduction, a dual-level control system is one means of providing the necessary pointing accuracy and stability for a large orbiting telescope. One conceptual technique for dual-level control is shown in figure 2.

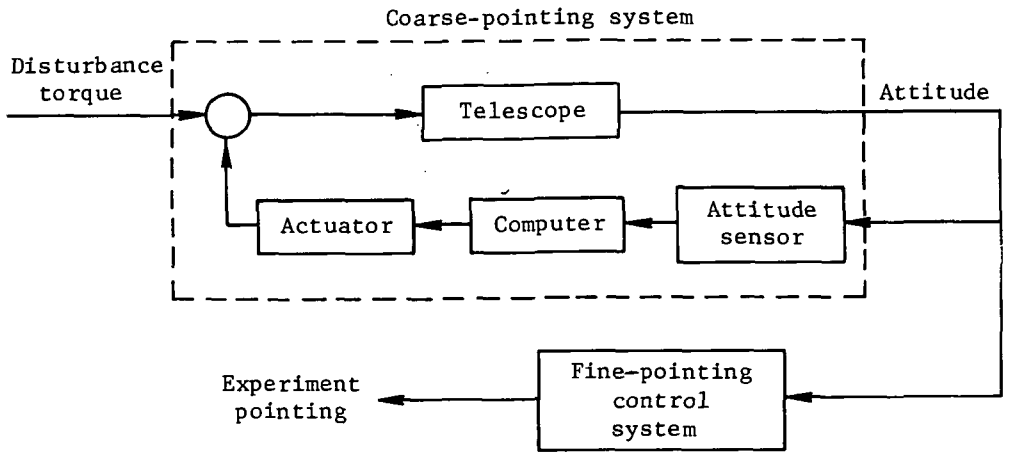

Figure 2.- Block diagram of dual-level control concept.

For the coarse-pointing system, a coarse star sensor provides attitude information for the attitude actuator. The actuator could be either an inertia wheel or a control moment gyro; the latter would be preferred for very large inertia bodies. The actuator provides a control torque to counteract the disturbance torque, thereby stabilizing the telescope structure within a coarse limit. The fine-pointing control system operates within the coarse-pointing limits to maintain all star images within the telescope field of view stabilized on the optical focal plane. In general, the fine-pointing control system includes a star sensor, controller, and plant – optical image motion compensator for this system – as shown in figure 3. In this figure, the variation in attitude of the vehicle

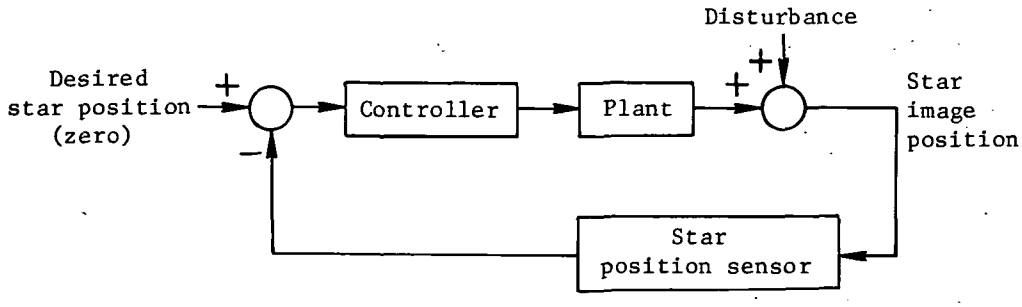

Figure 3.- Block diagram of generalized star image regulating technique.

while under control of the coarse-pointing system is shown as a disturbance input to the star image position in the focal plane.

In order to make the regulating system design specific, illustrative examples are presented in this paper. Table 1 contains system specifications that are used for the design. Other numbers are presented where applicable.

TABLE 1.- SYSTEM SPECIFICATIONS

Telescope aperture	3.05 m (120 in.)
f-number	100
Telescope focal length	305 m (12 000 in.)
Coarse-pointing accuracy	9.7×10^{-6} rad (2 arc sec)
Worst case input disturbance:	
Sine wave:	
Amplitude	2.91×10^{-7} rad (0.06 arc sec)
Frequency	0.5 Hz
Velocity	0.92×10^{-6} rad/sec
Fine-pointing accuracy goal	4.85×10^{-8} rad (0.01 arc sec)
Sampling period of digital sensor	0.01 sec
Desired fine-pointing system bandwidth	5 to 10 Hz
Guide-star magnitude	+10

A careful review of the literature (refs. 3 to 14) has indicated that these numbers are representative of the present problem; hence they will serve as a good basis for design.

Since the regulating system can be only as accurate as the star sensor, questions arise as to the type of transducer and measuring technique that might be used. Most available sensors work on some variation of the principle of physically dividing the focal plane in the vicinity of a star image into quadrants. When a star image is exactly centered in this region, all quadrants will have equal intensities. Any angular motion of the optical system will result in unequal intensities providing the basis for a highly sensitive analog nulling device. An obvious penalty of such a method is a very small linear range.

A technique for sensing star position was desired that is digital for ease of processing and computing, is capable of measuring errors rapidly, has a wide field of view that is easily adjustable, is linear over the complete range, has a simple measuring technique, and has the accuracy required for this application. In order to meet these requirements, a scanning technique that uses an image dissector tube as the transducer has been developed (ref. 15). Position information generated by the sensor is in the form of a digital number that represents the magnitude and direction of the star image displacement along the focal plane. At various time intervals, the digital number is shifted to an output register for use by the remaining portion of the control system. A more complete description of the operation of the star sensor, for the purpose of developing a mathematical model, is included subsequently.

The purpose of the optical portion of an image motion compensator is to provide a method for a control system to maintain a star image fixed on the focal plane despite small motions of the telescope axis. One technique that has been successfully employed is the transfer lens used in Stratoscope II (ref. 16). The main deficiency of this method is the residual aberrations caused by the lens.

Another technique involves the placement of a single flat mirror in the optical path. By rotating the mirror as the telescope moves, the image can be maintained fixed. Because the focal plane is effectively tied to the flat mirror, the focal plane must rotate by twice the angle that the mirror rotates through. The effect is twofold: First, the new focal plane is tilted relative to the original position; and second, the off-axis image is slightly behind the original focal plane. Therefore, the one-mirror technique can only control one star image over small angles without changing the focus.

A two-mirror image motion compensator that eliminates the focal plane problem has been designed and evaluated (ref. 17). The technique has the advantage that only two flat optical surfaces are required for two-axis control. An additional advantage is the ability to control all star images within the field of view simultaneously. A complete description of the operation and development of a mathematical model of the image motion compensator is included subsequently herein.

The controller includes a motor for driving the image motion compensator, a tachometer for damping, and electronics. The electronic system is mainly comprised of compensation which has been chosen both for stability considerations and for an adequate velocity-error constant. The compensation electronics also includes a digital-to-analog converter at the output of the star sensor and a zero-order hold. A direct-current, limited-motion, brushless, torque motor has been selected as the actuator to drive the image motion compensator. A mathematical model and description of the motor and rate loop are included subsequently. The next section describes the operation of each major component of the system and provides a basis for the development of mathematical models for the design.

Star Sensor

Description of operation.- This section contains a description of the star sensor used in the control system; the advantages of the sensor were described previously and are more completely described in reference 15. An image dissector tube is shown schematically in figure 4(a). A star image is focused on the front face of the tube which is located in the optical focal plane; this produces photoelectrons which are refocused onto the electron focal plane. The defining aperture, which is a slit for the single-axis case, is centered in the electron focal plane. The electron image is scanned vertically across the slit by passing a sweep signal through the magnetic deflection coils. A triangular sweep signal is plotted in figure 4(b) with the vertical axis representing the electron image position and the horizontal axis representing time. In this illustration the star image is off axis; therefore, the path of the electron image is not centered about

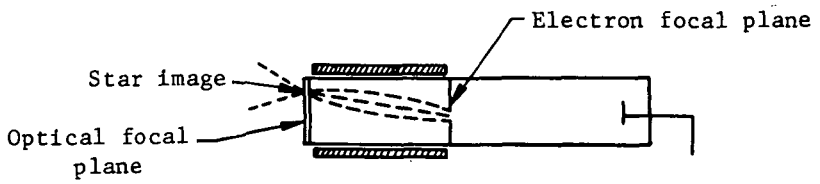

(a) Image dissector tube.

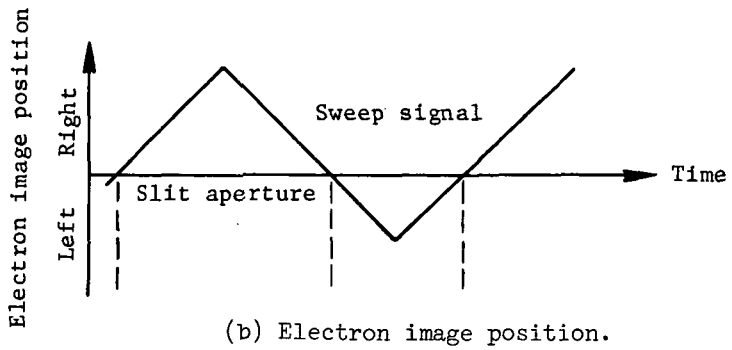

(b) Electron image position.

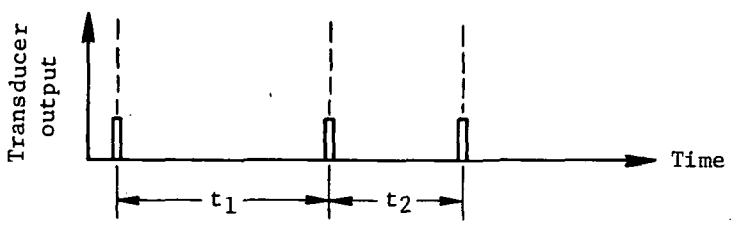

(c) Transducer output pulses.

Figure 4.- Schematic representation of image dissector tube and plots of sweep signal and output pulses.

the slit aperture. When the electron image crosses the slit, an electrical pulse will be generated. The pulses are shown idealized in figure 4(c). The time interval between successive pulses is measured by a precise clock reference, and the difference in the two times $(t_1$ and $t_2)$ is proportional to the angular error between the guide star and telescope. The sign of the resulting digital number indicates direction. Note that other symmetrical curves can be used for the sweep signal; however, the triangular sweep was selected because of the linear dependence of error on $t_2 - t_1$.

Mathematical model.- When the star image position is stationary on the optical focal plane, the measurement error is theoretically zero. When the image position changes with time, the star sensor exhibits a time lag, thereby causing a measurement error. Figure 5(a) contains representative waveforms illustrating the time history for

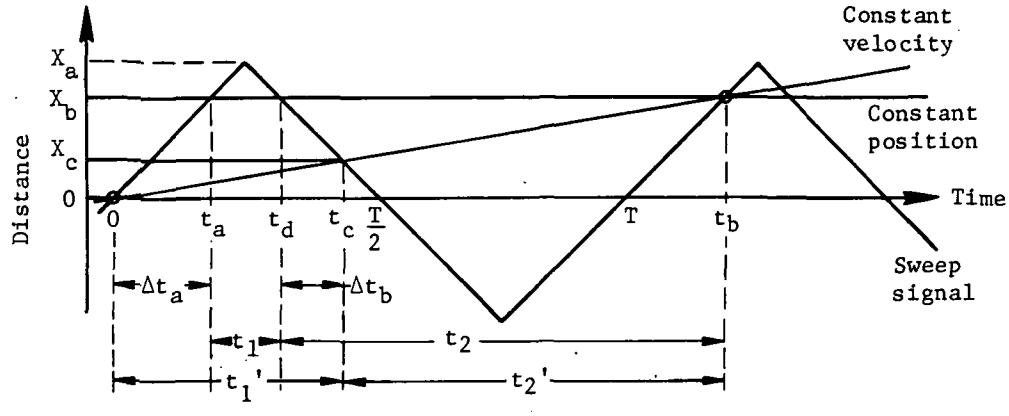

(a) Focal plane displacements for several waveforms.

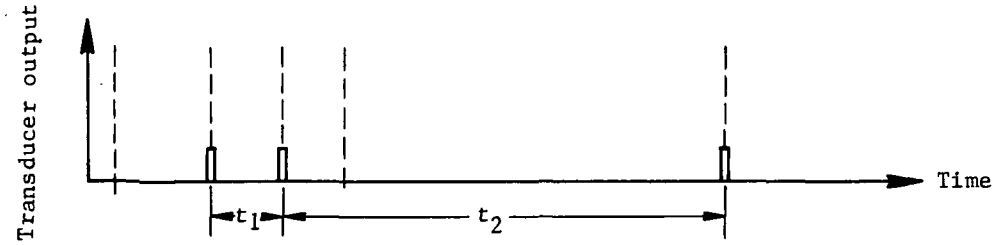

(b) Output pulses for constant position.

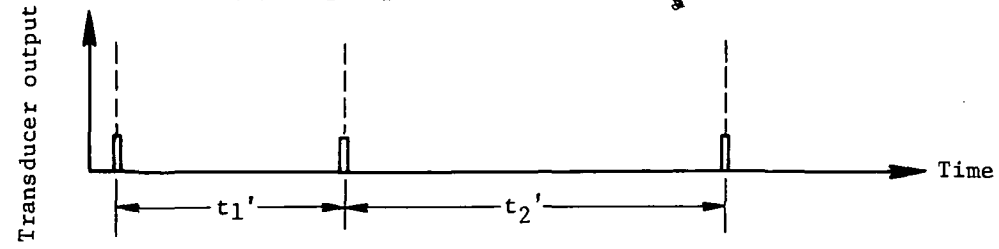

(c) Output pulses for constant velocity.

Figure 5.- Representative waveforms for cases of constant position and constant velocity with output pulses for each case.

a constant-position star image and for a star image moving with constant velocity. The lines for constant position and constant velocity represent a distance that is proportional to the electron voltage required to center the electron image. For example, X_b is the distance that the steady-state star is displaced in the optical focal plane and, hence, is proportional to the voltage required to center the electron image in the electron focal plane. Also, at time t_b, the star image moving with constant velocity m_d is displaced by a distance X_b in the optical focal plane. The sweep signal is shown to scan a distance X_a along the optical focal plane. The output pulses from the tube for the cases of constant position and constant velocity are shown in figures 5(b) and 5(c), respectively.

The attitude-measurement error ΔX_b for a constant-rate star image is derived in appendix A (eq. (A23)) as

$$\Delta X_b \approx \frac{2X_a}{R_m} \qquad \left(R_m >> 2; \quad R_m{}^2 >> 1\right) \tag{1}$$

where R_m is defined as

$$R_m = \frac{m_s}{m_d} \tag{2}$$

which is the ratio of the time rate of change of the sweep signal m_s to the time rate of change of the star image position m_d on the focal plane. Consequently, for a given X_a, the measurement error can be kept to an acceptable level by selecting the ratio R_m. Furthermore, for a worst case m_d, ΔX_b is directly related to the sweep period. (See eq. (A19) in app. A.) The peak amplitude X_a of the sweep signal may now be selected. It must be large enough to cover the complete field of view of the fine-pointing system. This amplitude can be determined by geometrical means. Since the focal length of the telescope is constant, the star image displacement X_d along the focal plane is proportional to the angular rotation ϕ of the telescope with respect to the guide star. For small angles of ϕ

$$X_d = K_f \phi \tag{3}$$

where K_f is a constant equal in magnitude to the focal length of the telescope. The required value of X_a is determined from equation (3) when ϕ is set equal to the maximum angular displacement that is to be controlled.

It is desired to model the digital star sensor for analysis. As indicated in appendix A, the steady-state error of the sensor model to a step of position would be zero (eq. (A1)); whereas the sensor output should follow a rate input disturbance with a constant-position error (eq. (1)). As shown in figure 6, the dynamic properties of the sensor can be modeled by a first-order time lag.

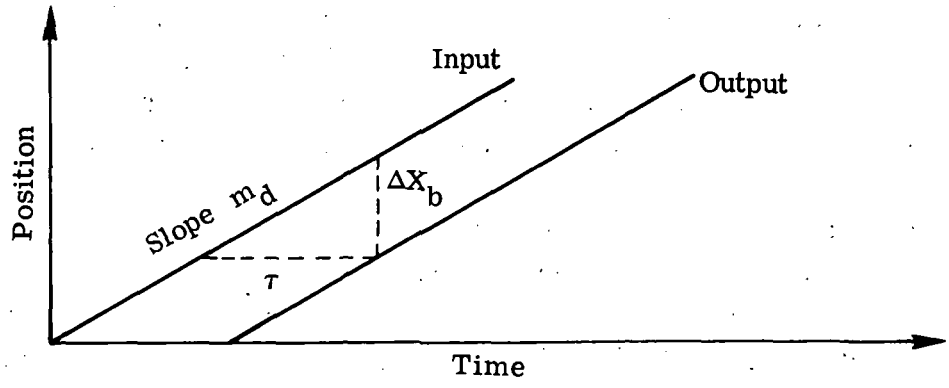

Figure 6.- Input disturbance and sensor output as function of time.

The time lag of the sensor model is defined as τ; the position error is ΔX_b; and the slope for both the input disturbance and output signal is m_d. From equation (A25) in appendix A, the time constant is

$$\tau = \frac{T}{2} \tag{4}$$

which relates the time constant to the sweep period of the star sensor. The mathematical model for the digital star sensor is shown in figure 7.

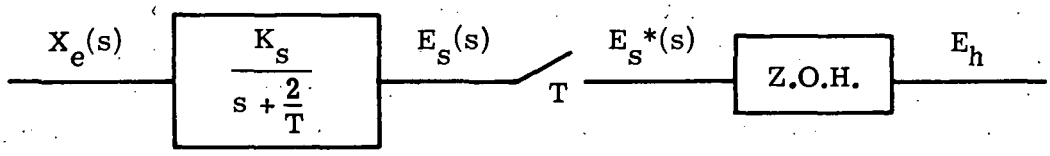

Figure 7.- Mathematical model of star sensor.

In deriving the mathematical model of the star sensor, the input quantity used was X_d, which is the component of image motion caused by the telescope attitude motion. In the intended application, a component of image motion also results from the action of the image motion compensator. The combined effect of the two motions yields the resultant star image position X_e on the optical focal plane. This input is converted to a proportional output signal E_s through a gain constant K_s. At the end of every sweep period T, the sensor output is transferred to a zero-order hold. The sampled sensor output is E_s^*, and the output from the zero-order hold is E_h.

As an example, a 3.05-meter (120-inch) telescope operating at f/100 has a focal length of 305 meters, thereby making K_s equal to 305 meters per radian. By using the fine-pointing field of view defined in table 1, 9.7×10^{-6} radian (2 arc sec), the amplitude X_a of the sweep signal must be at least 2.96 millimeters (eq. (3)). By assuming, as indicated in table 1, a worst case input disturbance of 2.91×10^{-7} radian in amplitude

and 0.5-hertz frequency, the maximum rate disturbance is approximately 0.92×10^{-6} radian per second. Based upon this rate disturbance and a focal length of 305 meters, the slope of the image m_d moving across the focal plane is 0.28 millimeter per second. The slope m_s is 1.18 meters per second based upon an amplitude of 2.96 millimeters and a period of 0.01 second (eq. (A19) in app. A). From equation (2), R_m is found to be 4214, thereby justifying the assumption made in equation (1). In the section entitled "Analog Computer Analysis," sinusoidal disturbance inputs with frequencies up to 20 hertz were simulated. For this extra conservative case, m_d is 11.15 millimeters per second and R_m is 106. For either case, with a period T of 0.01 second, the time constant τ becomes 0.005 second (eq. (4)).

Image Motion Compensator

Description of operation.- As indicated in the section entitled "General System Description," it is desirable to have an image motion compensator which has the capability of handling two or more star images without altering the focal plane. A device with these features has been developed for this application and is more completely described in reference 17. A schematic representation of a two-mirror image motion compensator is shown in figure 8. In figure 8(a), rays from a star are imaged on the focal plane after reflecting from two plane parallel mirrors. During actual operation the telescope will move, thereby causing all star images in the telescope field of view to be moved on the focal plane. The two mirrors will then be rotated and translated to bring the star images back to the original position. For ease of experimental evaluation and discussion, the telescope has been assumed to be stationary and the star image motion on the focal plane has been analyzed as a function of mirror rotation only. First, the two mirrors must be maintained parallel to each other as they are rotated so as to prevent the focal plane from tilting. By doing this, all stars within the field of view will be imaged on a plane that is parallel to the original focal plane, but the star images will be changed in focus. Second, the change in focus can be eliminated if the path length from the top mirror to the focal plane is maintained constant. This can be accomplished by translating the bottom mirror as it is rotated as shown in figure 8(b). Both mirrors have been rotated through the same angle, and the image has been translated along the focal plane. The distance between the two mirrors has been changed, but the total path length remains constant. It can be shown that the bottom mirror is always tangent to a parabola and the top mirror rotates on the focus of the parabola.

The hardware used to demonstrate the single-axis technique is shown in figure 9, which is a complete assembly of the two-mirror system. The two mirrors are mounted on a common plate to maintain parallelism. One of the two mirrors is mounted on a linear-motion bearing to vary the distance between the mirrors; the distance is regulated by a guide mounted on the base below. The guide functions as the directrix of the

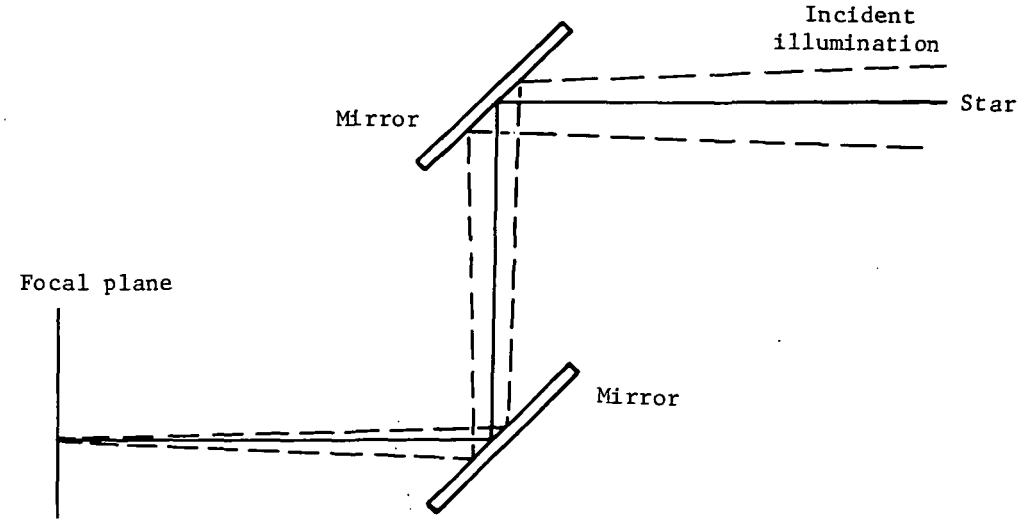

(a) Initial alinement.

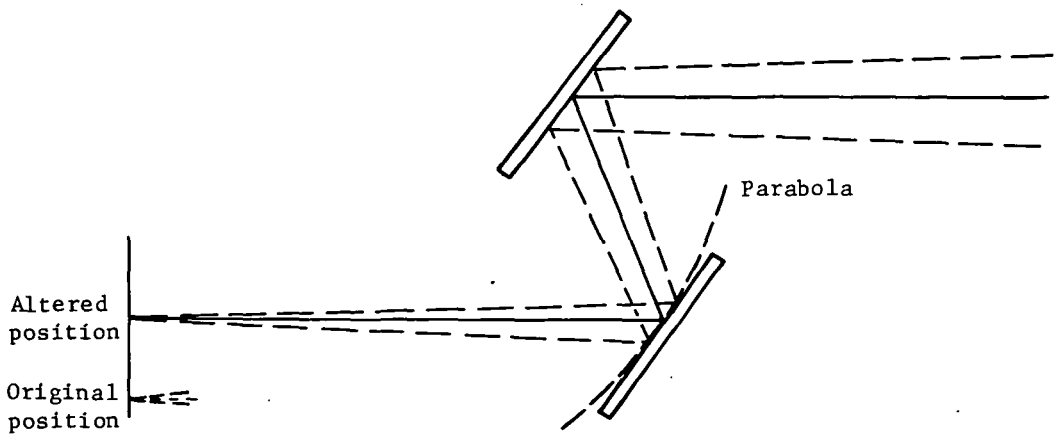

(b) Rotated mirror position.

Figure 8.- Schematic representation of image motion compensator.

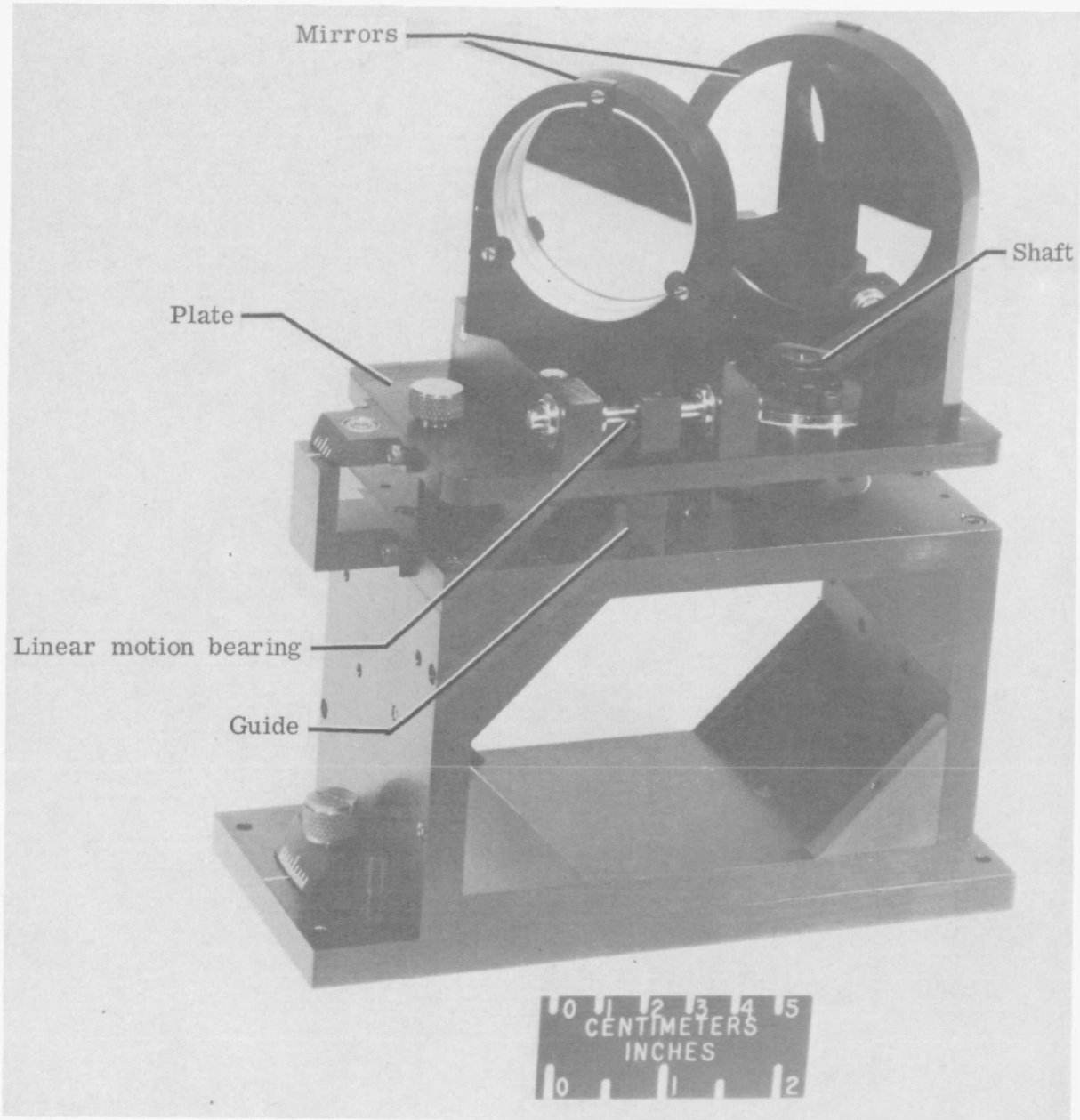

L-69-2322.1

Figure 9.- Image motion compensator.

parabola, and the shaft, which is the center of rotation of the common plate, serves as the focus. A more detailed description is given in reference 17.

The previous discussion handles the single-axis case and is sufficient to demonstrate the feasibility of the technique. This technique can be extended to the requisite two-axis system with the following changes. The main change is that one of the mirrors should be tangent to a surface that is a paraboloid of revolution. As shown in figure 10, motions in the X-Y plane are parabolic, while those in the X-Z plane are circular. Two mirrors will be sufficient for two-axis control. For the purpose of this study, only a single-axis case is considered with motion in the X-Y plane, and all displacements are along the X-axis.

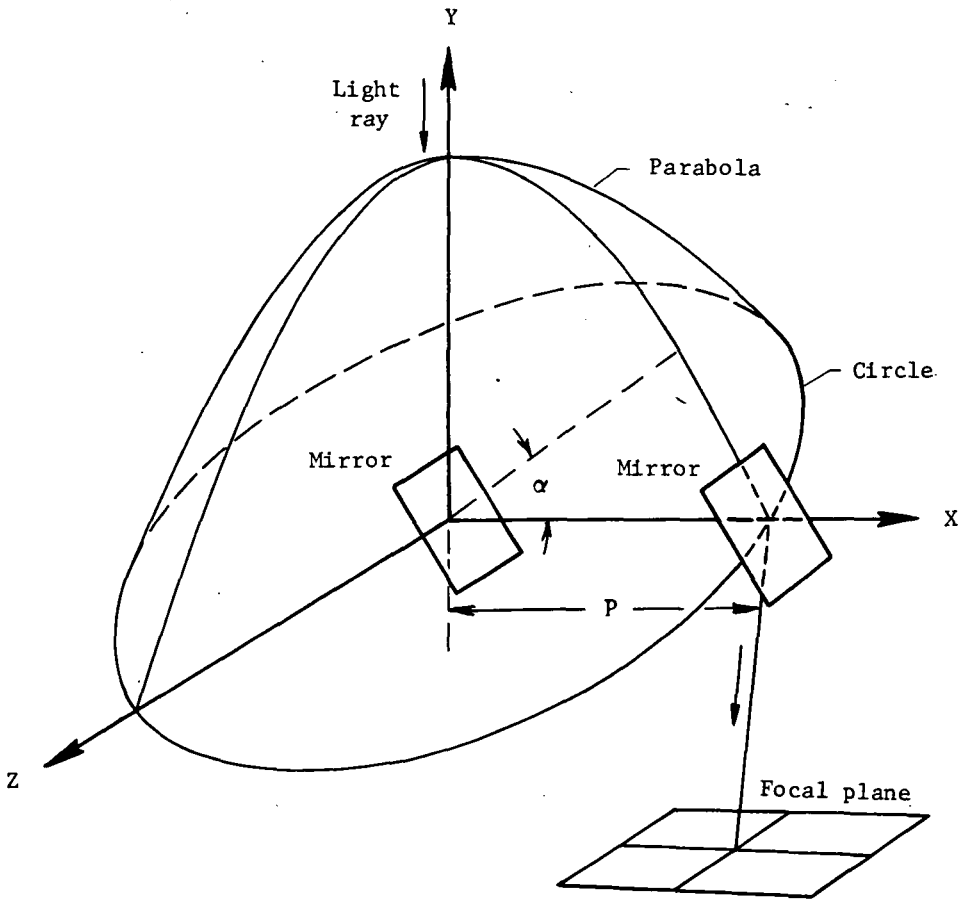

Figure 10.- Schematic diagram illustrating two-axis technique.

Mathematical model.- The displacement of the star image is a function of the angular rotation α of the two mirrors. The following equation describes the relationship as

$$X_p = \frac{2P \tan \alpha}{1 + \tan \alpha} \qquad (\alpha \neq -45^o, 135^o) \qquad (5)$$

(see eq. (3) of ref. 17 where X_p is called $\overline{IH}$ and P is called p) where X_p is the star image displacement caused by mirror rotation, and P is the distance between the two mirrors when they are both at an angle of 45^o to the optic axis. For small values of α, X_p can be approximated by

$$X_p \approx K_m \alpha \tag{6}$$

where K_m is assumed to be a constant equal to 2P. The maximum value of α is determined by the worst case telescope disturbance – stability of the coarse-pointing control system – and is proportional to X_d, which is calculated by using equation (3). The mirrors are rotated in a direction to produce an X_p, which compensates for the image motion X_d produced by angular motion of the telescope. The relationship is

$$X_e = X_d - X_p \tag{7}$$

where X_e is the resultant star image displacement on the focal plane. Consequently, once the maximum value of X_d is determined from equation (3), the maximum value of α can be determined from equation (6). The model representing equations (3), (6), and (7) is shown in figure 11.

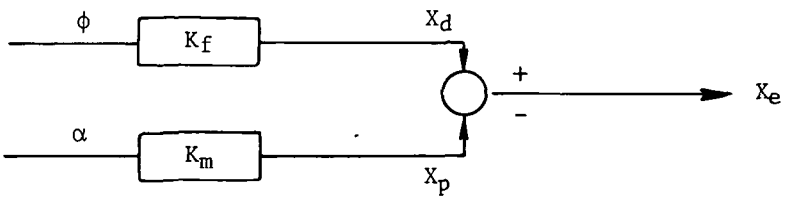

Figure 11.- Mathematical model of star image motion compensator. Transfer function for input disturbance.

As an example, the maximum value of X_d, which is equivalent to X_a, has previously been calculated as 2.96 millimeters (0.117 inch) for ϕ of 9.7×10^{-6} radian. The maximum value of α required to compensate for this displacement is 0.03 radian (1.717^o) for α positive and 0.028 radian for α negative and is based on P equal to 50.8 millimeters (2 inches). Figure 12 contains a plot of X_p as a function of α and is based upon equation (5). The curve has been plotted over a range of α of ±0.035 radian ($\pm 2^o$). Comparison with equation (6), where K_m is equal to 0.1016 meter per radian, reveals a peak error of 3 percent over the required angular range.

Direct-Current Torque-Motor Equations and Modeling of Rate Loop

A direct-current, limited-motion, brushless torque motor has been selected as the actuator to provide the rotational input to the image motion compensator. The torque motor is suited to this application for the following reasons: It possesses (1) infinite angular resolution, (2) limited but sufficient angular range, (3) reasonable torque levels,

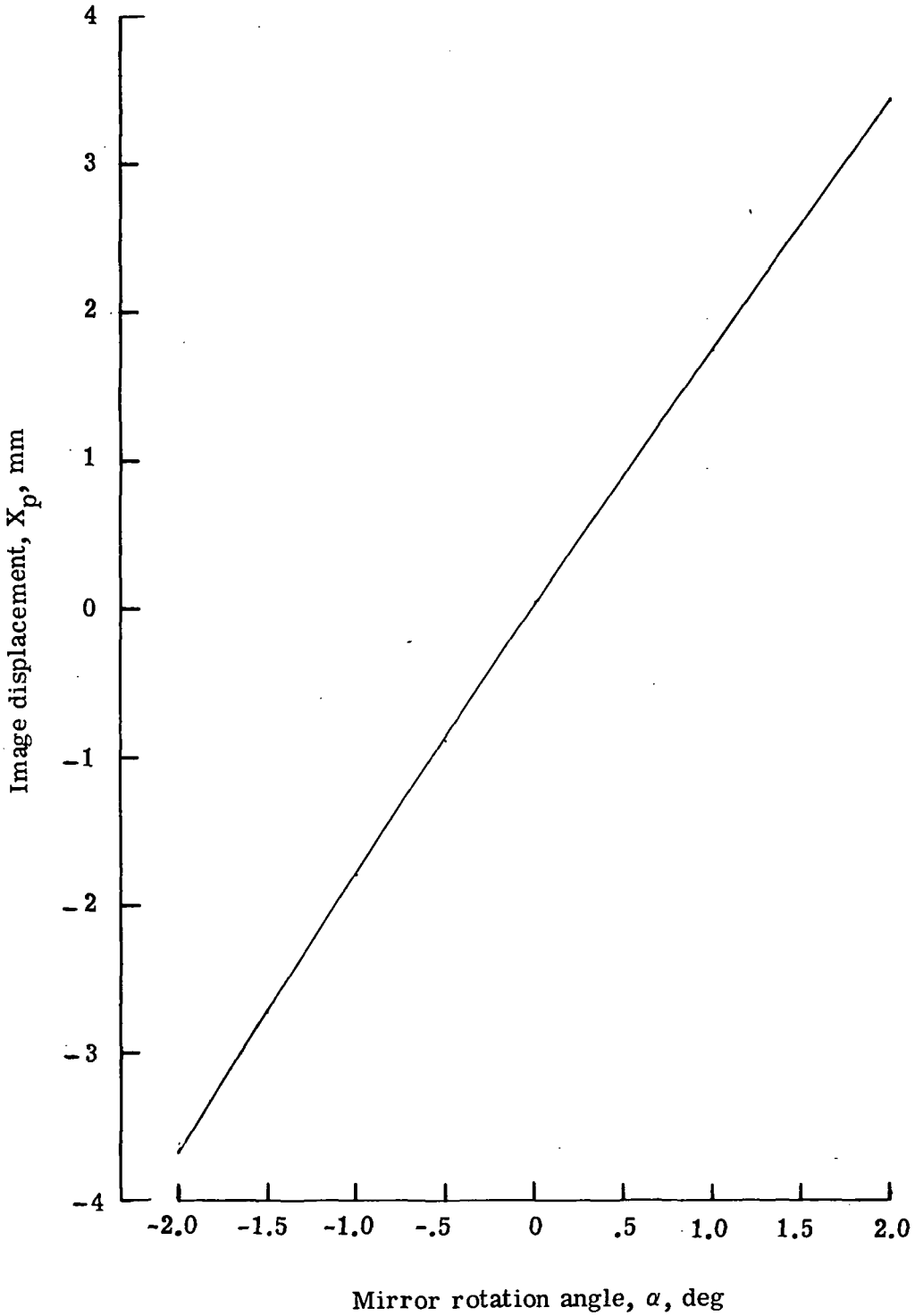

Figure 12.- Plot of star image displacement as function of mirror rotation angle.

and (4) extremely low friction levels because the only physical contact to the rotor is through precision bearings. A block diagram for the loop is shown in figure 13, and the circuit diagram is shown in figure 14. Typical derivations of the transfer function for this rate loop can be found in many textbooks. (For example, see ref. 18.) For this reason, only a general description of the loop and a few key equations are presented.

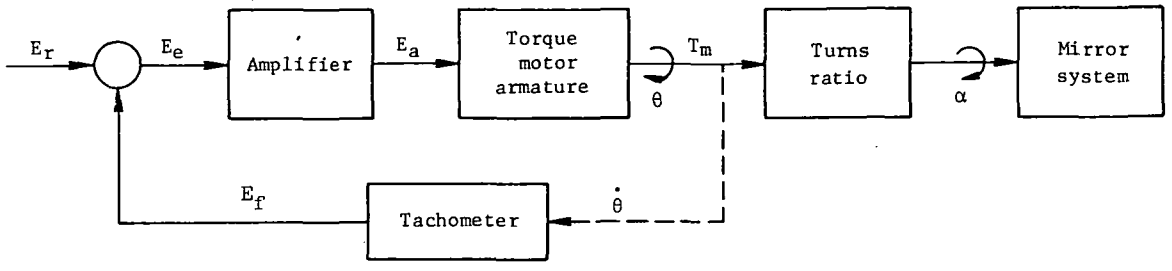

Figure 13.- Block diagram of rate loop.

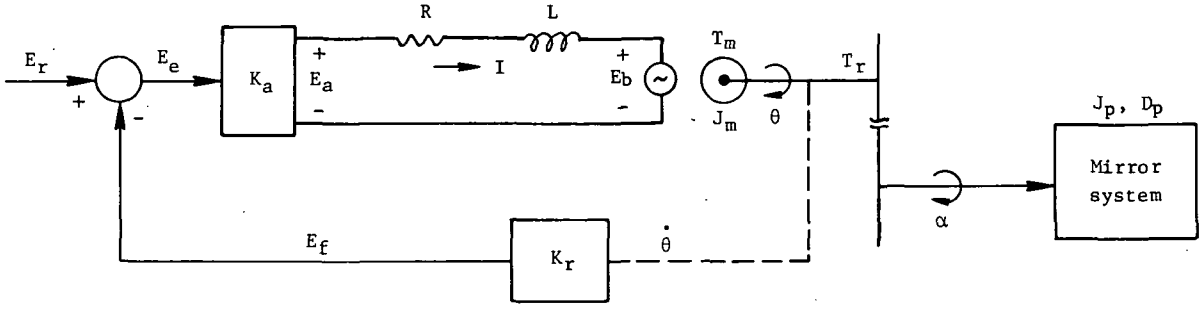

Figure 14.- Circuit diagram of rate loop.

The input voltage E_r to the rate loop is a function of the star image displacement X_e on the optical focal plane. The input voltage is summed with the feedback E_f generated by the tachometer with gain K_r producing an error signal E_e, which is then amplified by gain K_a and applied to the stator winding of the motor. The torque T_m generated by the motor is used to drive the load, which consists of motor inertia J_m and image motion compensator inertia J_p. Because high-quality bearings have been selected, viscous damping of the image motion compensator is extremely small compared with the total damping of the rate loop and is neglected. The Laplace transform transfer function relating the angular rotation of the motor θ to the input voltage is

$$\theta(s) = \frac{\frac{R}{L}J_L}{s}\left[\frac{\frac{K_aK_t}{R}E_r(s)}{s^2 + \frac{R}{L}s + \frac{R}{L}\left(\frac{B}{J_L} + \frac{K_aK_tK_r}{RJ_L}\right)}\right] \tag{8}$$

where R and L are the resistance and inductance of the torque motor, respectively. The viscous-damping term B is a function of the winding resistance, torque-motor sensitivity constant K_t, and torque-motor back emf constant K_b as

$$B = \frac{K_b K_t}{R} \tag{9}$$

and the total-system inertia J_L is

$$J_L = J_m + \frac{J_p}{n^2} \tag{10}$$

where n is the turns ratio relating θ to the mirror angle α. Physically, this ratio is obtained from a mechanical linkage consisting of a combination of solid rods and precision instrument bearings, thereby eliminating backlash problems associated with gears.

In the actual design, a torque motor, which has a very small electrical time constant (L/R) on the order of 0.003 second, has been chosen. For a negligible time constant, equation (8) reduces to

$$\theta(s) = \frac{\frac{K_a K_t}{J_L R} E_r(s)}{s\left(s + \frac{B}{J_L} + \frac{K_a K_t K_r}{J_L R}\right)} \tag{11}$$

which is the closed-loop transfer function used in the design.

For purpose of illustration, some gain constants used in the actual design are shown in table 2. By using these gain constants, the transfer function in equation (11) becomes

$$\theta(s) = \frac{4200 E_r(s)}{s(s + 128)} \tag{12}$$

where the break frequency is 128 radians per second.

TABLE 2.- GAIN CONSTANTS FOR RATE LOOP

K_a, V/V	1000
K_t, N-m/A	0.593
R, ohms	10
B, $\frac{\text{N-m-sec}}{\text{rad}}$	0.0344
J_L, $\frac{\text{N-m-sec}^2}{\text{rad}}$	0.0141
K_r, $\frac{\text{V-sec}}{\text{rad}}$	0.03

The mathematical models developed in this section are combined to form a complete control system. In the next section, the open-loop gain, break frequencies, and compensation are determined.

DESIGN ANALYSIS

Effective utilization of the mathematical models that have been developed requires the proper selection of gains and break frequencies and the design of compensation. The worst case input disturbance representing the attitude variation of the telescope is assumed to be a sine wave with a frequency of 0.5 hertz and an amplitude of 2.91×10^{-7} radian (table 1). In order to insure adequate response of the control system at the maximum disturbance frequency, the fine-pointing control system should have a bandwidth approximately 10 times greater than the maximum input frequency; hence, a 5- to 10-hertz bandwidth has been established. Corresponding to the worst case input disturbance, the maximum rate disturbance is approximately 0.92×10^{-6} radian per second. The control system is required to follow these rates with a steady-state position error less than 4.85×10^{-8} radian while guiding on a +10-magnitude star.

The design approach is first to assume a continuous-data network to establish approximate loop gains, break points, and required compensation. The main objective of the continuous-data analysis, using the familiar s-plane techniques, is to obtain a compensatory network which will cause the discrete system to perform approximately as specified. By using z-transform theory, the behavior of the discrete system with this compensation is checked and, if necessary, modifications are made. Next, the gains and compensation established from the analysis are tested in the analog computer simulation, which includes sensor noise. Finally, the complete control system is experimentally tested by using actual hardware.

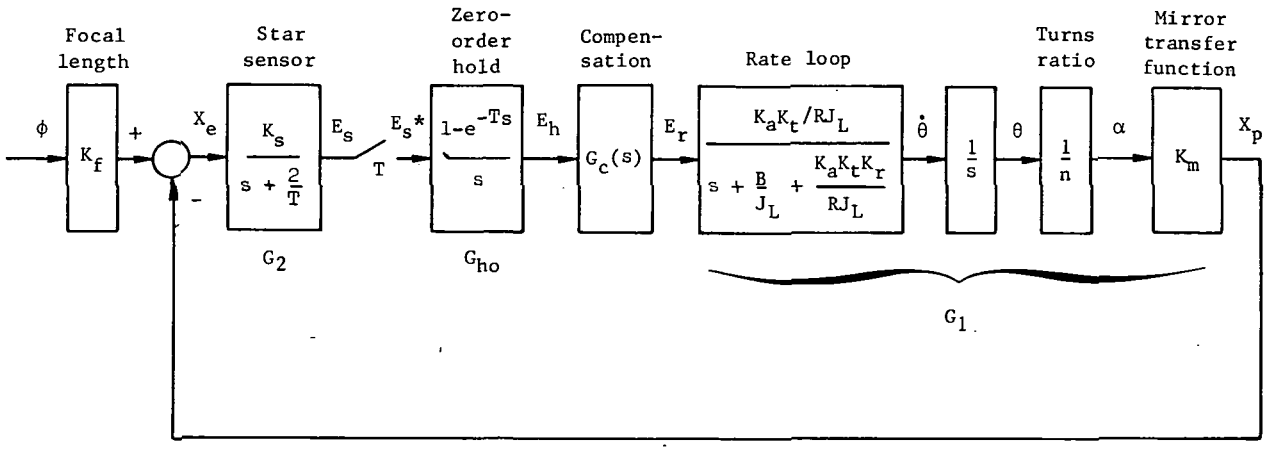

Figure 15.- Block diagram representing mathematical model of control system.

Continuous-Data Approximation

A block diagram representing the mathematical model of the control system is shown in figure 15. By using block-diagram manipulation techniques (ref. 18), block G_2 can be removed from the forward path and inserted in the input path and in the feedback path. Block G_2 can then be transferred through the output junction into the forward loop on the right of the sampler and into the output path where it appears in inverted form as $1/G_2$. For this configuration the open-loop pulse transfer function of the closed-loop portion of the control system is

$$G_{ho}G_cG_1G_2^*(j\omega) = \frac{1}{T}\sum_{m=-\infty}^{\infty}\left[G_{ho}(j\omega + jm\omega_s)\, G_c(j\omega + jm\omega_s)\, G_1(j\omega + jm\omega_s)\, G_2(j\omega + jm\omega_s)\right] \tag{13}$$

where G_{ho} represents the zero-order hold, G_c is the compensator, G_1 includes the rate loop and mirror transfer function, G_2 is the star sensor, and ω_s is the sampling frequency. The transfer function of the zero-order hold is

$$G_{ho}(j\omega) = T\,\frac{\sin\left(\frac{1}{2}\omega T\right)}{\frac{1}{2}\omega T}\,e^{-\frac{j\omega T}{2}} \tag{14}$$

Substitution of equation (14) into equation (13) yields

$$G_{ho}G_cG_1G_2^*(j\omega) = \frac{1}{T}\sum_{m=-\infty}^{\infty}\left[T\,\frac{\sin\frac{\omega + m\omega_s}{2}T}{\frac{\omega + m\omega_s}{2}T}\,e^{-\frac{j(\omega+m\omega_s)T}{2}} \times G_c(j\omega + jm\omega_s)\, G_1(j\omega + jm\omega_s)\, G_2(j\omega + jm\omega_s)\right] \tag{15}$$

Since the required frequency response of the control system must be below 10 hertz (63 radians per second), which is one-tenth of the basic sampling frequency ω_s, the pulse transfer function can be approximated by the first term of the expansion series (ref. 19). Furthermore, the sampler and zero-order hold have a magnitude nearly equal to one and are approximated by a pure time lag of one-half the sampling period T. By using these approximations, the transfer function becomes

$$G_{ho}G_cG_1G_2^*(j\omega) = e^{-\frac{j\omega T}{2}}\, G_c(j\omega)\, G_1(j\omega)\, G_2(j\omega) \tag{16}$$

A block diagram of the linear continuous-data approximation is shown in figure 16. For the continuous system, block G_2 in the input path and block $1/G_2$ in the output path

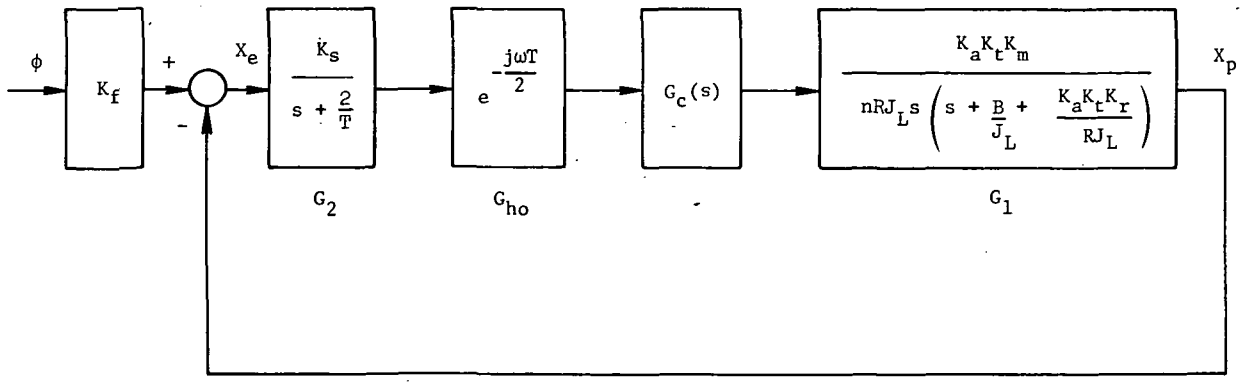

Figure 16.- Continuous-system approximation of discrete control system.

cancel. The continuous-data system represents a unity feedback, type-one control system. By assuming stability, the steady-state position error for this system can be determined from the final-value theorem as

$$\lim_{t\to\infty} X_e(t) = \lim_{s\to 0} \frac{s\phi(s)\, K_f}{1 + G_1(s)\, G_2(s)\, G_c(s)\, G_{ho}(s)} \tag{17}$$

where $\phi(s)$ represents the input disturbance, $G_{ho}(s)$ has a steady-state gain of one, and $G_c(s)$ has a steady-state gain of K_c. For a velocity input with magnitude ϕ_o the steady-state position error is

$$\lim_{t\to\infty} X_e(t) = \frac{\phi_o K_f}{K_V} \tag{18}$$

where K_V is the velocity-error constant, which is

$$K_V = \frac{K_s K_c K_a K_t K_m}{nRJ_L\left(\frac{2}{T}\right)\left(\frac{B}{J_L} + \frac{K_a K_t K_r}{RJ_L}\right)} \tag{19}$$

The next step in the preliminary analysis is to determine the break frequency for the rate loop and choose the compensation. The break frequency for the star sensor has previously been established as 2/T radians per second. The break frequency for the rate loop is selected by considering such items as stability and the physical properties of the torque motor and load. From a stability viewpoint, it is desirable for the break frequency to have a higher frequency than the bandpass frequency. From a practical viewpoint, the break frequency should not be too high so as to insure that the assumption of a negligible torque-motor winding-time constant is valid.

One other area of interest is to insure adequate phase margin β_m for the control system. The phase margin is defined as

$$\beta_m = 180 - \beta_c \tag{20}$$

where β_c is the phase shift of the open-loop system at the crossover frequency. By assuming a compensator with a first-order break frequency in the numerator and denominator, the phase shift can be calculated as

$$\beta_c = \tan^{-1}\frac{\omega_c}{\omega_1} - \tan^{-1}\frac{\omega_c}{\omega_2} - \tan^{-1}\frac{\omega_c}{\omega_3} - \tan^{-1}\frac{\omega_c}{\omega_4} - \frac{\pi}{2} - \frac{\omega_c T}{2} \tag{21}$$

where ω_1 and ω_2 represent the numerator and denominator break frequencies for the compensator, ω_3 is the break frequency for the rate loop, ω_4 is the break frequency for the sensor, and ω_c is the crossover frequency. Each trigonometric term in equation (21) can be represented by a power series as (ref. 20)

$$\tan^{-1}\frac{\omega_c}{\omega_i} = \frac{\omega_c}{\omega_i} - \frac{1}{3}\left(\frac{\omega_c}{\omega_i}\right)^3 + \frac{1}{5}\left(\frac{\omega_c}{\omega_i}\right)^5 - \ldots \qquad \left(\frac{\omega_c}{\omega_i} < 1\right) \tag{22a}$$

$$\tan^{-1}\frac{\omega_c}{\omega_i} = \frac{\pi}{2} - \frac{\omega_i}{\omega_c} + \frac{1}{3}\left(\frac{\omega_i}{\omega_c}\right)^3 - \frac{1}{5}\left(\frac{\omega_i}{\omega_c}\right)^5 + \ldots \qquad \left(\frac{\omega_c}{\omega_i} > 1\right) \tag{22b}$$

where $i = 1, 2, 3, 4$. Since the power series converges rapidly for most values of the argument, the first-order terms are adequate as

$$\tan^{-1}\frac{\omega_c}{\omega_i} \approx \frac{\omega_c}{\omega_i} \qquad \left(\frac{\omega_c}{\omega_i} < 1\right) \tag{23a}$$

$$\tan^{-1}\frac{\omega_c}{\omega_i} \approx \frac{\pi}{2} - \frac{\omega_i}{\omega_c} \qquad \left(\frac{\omega_c}{\omega_i} > 1\right) \tag{23b}$$

where $i = 1, 2, 3, 4$. Equation (21) can now be written by using the form of equations (23) as

$$\beta_c = -\frac{\pi}{2} - \frac{\omega_c T}{2} + \left(\frac{\pi}{2} - \frac{\omega_1}{\omega_c}\right) - \left(\frac{\pi}{2} - \frac{\omega_2}{\omega_c}\right) - \frac{\omega_c}{\omega_3} - \frac{\omega_c}{\omega_4} \tag{24}$$

where the crossover frequency is assumed to be greater than the break frequencies of the compensator and is lower than the break frequencies of the rate loop and sensor.

As in previous sections, an example will be used to establish the design for this system. The control system is required to follow a rate input disturbance θ_o of 0.92×10^{-6} radian per second with a maximum star image position error of $4.85 \times 10^{-8} K_f$ meter (table 1). By using equation (18), the minimum value for K_V is 19 per second. Because the preliminary analysis neglects sensor noise and approximates the sampler and zero-order hold, a steady-state position error three times better than required is used. For this safety factor, K_V becomes 57 per second. The sensor break frequency is determined by the sampling period. For T equal to 0.01 second (table 1), the break frequency becomes 200 radians per second. The break frequency of the rate loop must be higher than the bandpass frequency, which is specified to be a maximum of 10 hertz. A break frequency of 128 radians per second has been selected to satisfy the requirements outlined previously. A Bode plot of the uncompensated open-loop system is shown in figure 17. Since an approximate control system is being evaluated, a conservative phase margin of 50^o minimum has been chosen; this implies a phase shift of 130^o at unity gain. For the uncompensated case, ω_1 and ω_2 are zero, ω_c is 57 radians per second, and β_c is therefore determined from equation (24) to be 149^o. The desired phase shift can be obtained by decreasing the crossover frequency to 32 radians per second, which is the minimum acceptable bandpass of the closed-loop system, while maintaining K_V at 57 per second. Because the crossover frequency has been decreased by a factor of 0.56, the attenuation must result from the compensation. For a first-order compensator, the break frequencies are approximately linearly related to the attenuation. Thus, the relationship between ω_1 and ω_2 is

$$\omega_2 = 0.56\omega_1 \tag{25}$$

If this relationship is substituted into equation (24) with β_c equal to -130^o and ω_c equal to 32 radians per second, ω_1 becomes approximately 8 radians per second and ω_2 is 4.5 radians per second. A Bode plot for the compensated system is shown in figure 17.

Thus, by using the indicated compensation, the approximate continuous-data system has a K_V of 57 per second, an open-loop crossover frequency of 32 radians per second (3-decibel point is 46 radians per second), and a phase margin of 50^o. The next section provides a check on the general operating characteristics of the system by using z-transform theory.

Discrete-Data System

The break frequencies established in the continuous-data system can now be checked by using z-transform theory. The approach used is to transform from the s-plane to the z-plane, check the stability of the system by plotting the root locus of the characteristic equation, and evaluate the general operating characteristics at the design gain.

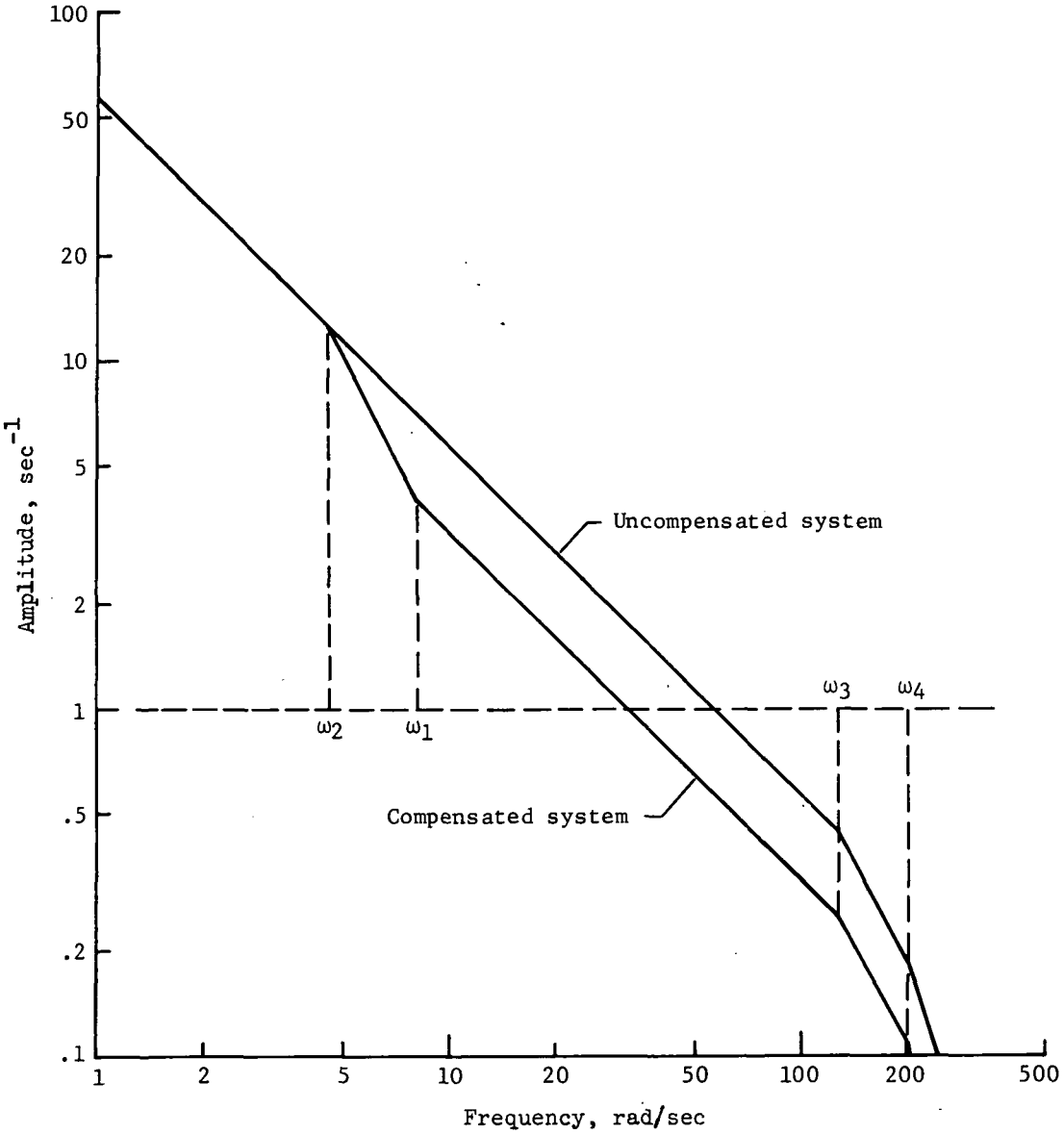

Figure 17.- Bode plot for continuous-system approximation.

The block diagram for the sampled-data control system has previously been shown in figure 15. For convenience, the gain constants are lumped together and designated as K. The z-transform for the output signal $Z(X_p)$ is derived in appendix B (see eq. (B8)) as

$$Z(X_p) = X_p(z) = \frac{K\left[K_f\phi\ G_2(z)\right]\ G_3(z)}{1 + KG_2\ G_3(z)} \tag{26a}$$

where

$$K_f\phi\ G_2(z) = Z\left[\frac{K_f\phi(s)}{s + \omega_4}\right] \tag{26b}$$

$$G_3(z) = G_{ho}G_cG_1(z) = Z\left[\frac{(1 - e^{-Ts})(s + \omega_1)}{s^2(s + \omega_2)(s + \omega_3)}\right] \tag{26c}$$

and

$$KG_2\ G_3(z) = Z\left[\frac{K(1 - e^{-Ts})(s + \omega_1)}{s^2(s + \omega_2)(s + \omega_3)(s + \omega_4)}\right] \tag{26d}$$

The stability of the control system is determined from the characteristic equation

$$1 + KG_2\ G_3(z) = 0 \tag{27}$$

From z-transform theory

$$z = e^{Ts} \tag{28}$$

and equation (26d) reduces to

$$KG_2\ G_3(z) = K(1 - z^{-1})Z\left[\frac{s + \omega_1}{s^2(s + \omega_2)(s + \omega_3)(s + \omega_4)}\right] \tag{29}$$

The z-transform in equation (29) can be found by expanding the terms inside of the brackets by the method of partial fractions, thereby yielding

$$KG_2\ G_3(z) = K(1 - z^{-1})Z\left(\frac{C_a}{s^2} + \frac{C_b}{s} + \frac{C_c}{s + \omega_2} + \frac{C_d}{s + \omega_3} + \frac{C_e}{s + \omega_4}\right) \tag{30}$$

where C_a, C_b, C_c, C_d, and C_e are the residues. The z-transform for each partial fraction in equation (30) is shown in appendix B (eq. (B13)). Substitution of these transforms into equation (30) and use of equation (27) results in the characteristic equation

$$1 + K\left(1 - z^{-1}\right)\left[\frac{C_a T z}{(z-1)^2} + \frac{C_b z}{z-1} + \frac{C_c z}{z - e^{-\omega_2 T}} + \frac{C_d z}{z - e^{-\omega_3 T}} + \frac{C_e z}{z - e^{-\omega_4 T}}\right] = 0 \tag{31}$$

where the residues are defined in appendix B (eqs. (B18a) to (B18e)).

The velocity-error constant can be derived from equation (31) for a stable system by applying the final-value theorem for z-transforms. The equation for the velocity-error constant is derived in appendix B (eq. (B24)) as

$$K_V = \frac{1}{T} \lim_{z \to 1} \left[(z - 1) K G_2 G_3(z)\right] \tag{32}$$

Equations (31) and (32) are combined to yield

$$K_V = K C_a \tag{33}$$

The z-transform root locus of the nonapproximate system has been plotted for equation (31) by using the numerical values of break frequencies that were determined from the continuous-system approximation as follows: (1) ω_1 is 8 radians per second; (2) ω_2 is 4.5 radians per second; (3) ω_3 is 128 radians per second; (4) ω_4 is 200 radians per second; and (5) T is 0.01 second. By using these values, the characteristic equation is

$$1 + K G_2 G_3(z) = 1 + K\left(2.202 \times 10^{-20}\right)\left[\frac{(z + 0.1096)(z + 1.808)(z - 0.923)\left(z + 3.616 \times 10^{12}\right)}{(z - 0.135)(z - 0.278)(z - 0.956)(z - 1)}\right] \tag{34a}$$

where

$$K_V = \frac{K}{14\,400} \tag{34b}$$

The root-locus plot for equations (34) is shown in figure 18. The crosses in figure 18 represent the open-loop poles, the circles represent the open-loop zeros, and the squares are the location of the closed-loop poles for the gains K_V specified in the figure. Because the root locus is symmetrical about the real axis, only the upper portion of the z-plane has been plotted. For the selected gain of 57 per second, the damped natural frequency ω_d for the oscillatory poles is approximately 44 radians per second, and the damping ratio ζ is 0.62. Both ω_d and ζ are shown in figure 18. The control system becomes unstable when the roots of the characteristic equation leave the unit circle; the gain at this point is 234 per second.

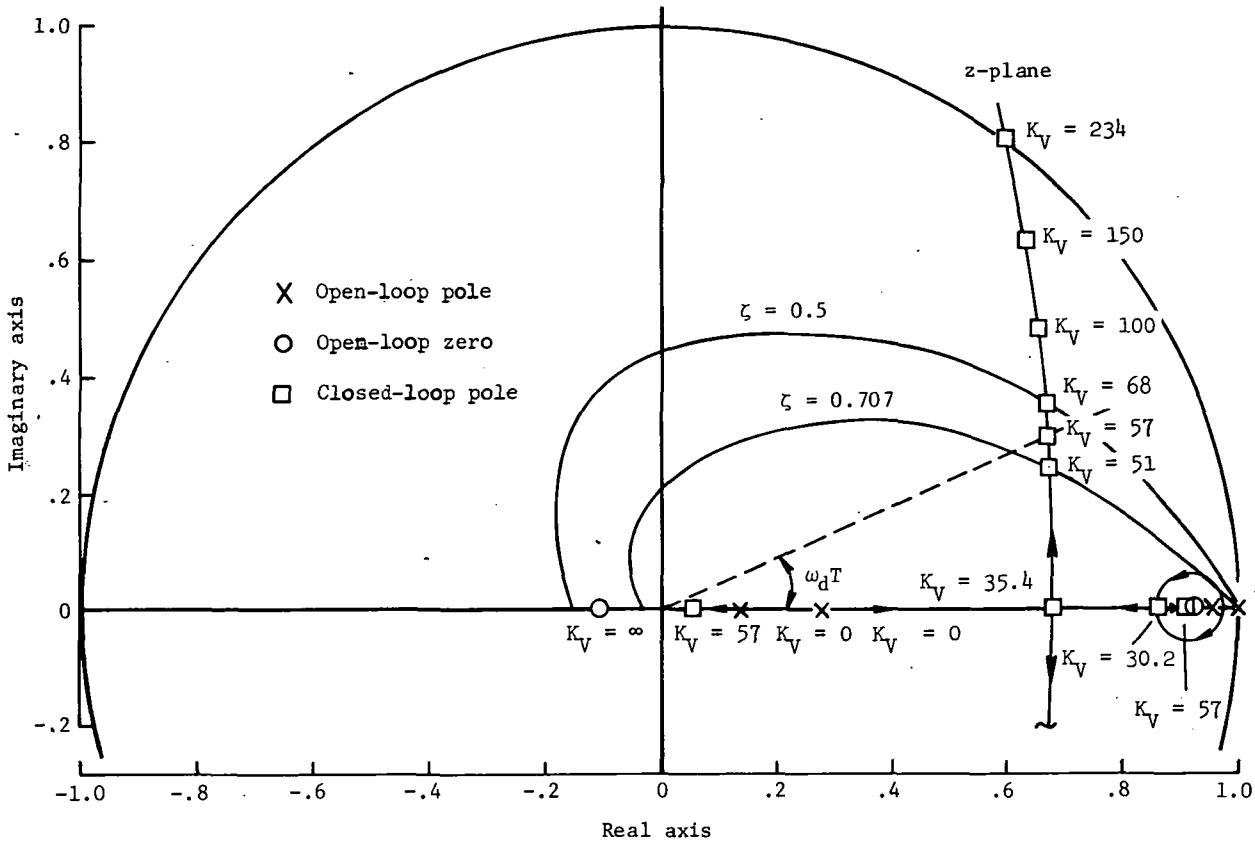

Figure 18.- z-transform root locus for system with (s + 8)/(s + 4.5) compensation.

The net effect of the compensation is to add a pole-zero combination of 0.956 and 0.923, respectively. This combination caused the small circular locus shown in figure 18 and allowed a larger K_V without significantly changing the damped natural frequency or damping ratio as obtained in the uncompensated case. For comparison, the root locus has been plotted in figure 19 for the uncompensated system. The characteristic equation for this case is

$$1 + KG_2\,G_3(z) = 1 + K\left(1.69 \times 10^{-21}\right)\left[\frac{(z + 0.109)(z + 1.79)\left(z + 4.65 \times 10^{13}\right)}{(z - 0.135)(z - 0.278)(z - 1)}\right] \tag{35a}$$

where

$$K_V = \frac{K}{25\,600} \tag{35b}$$

As previously pointed out, the mathematical model assumes a constant sampling period and does not include sensor noise. In view of these facts and the fact that the compensation has very little effect on the root locus other than an increase in K_V, the

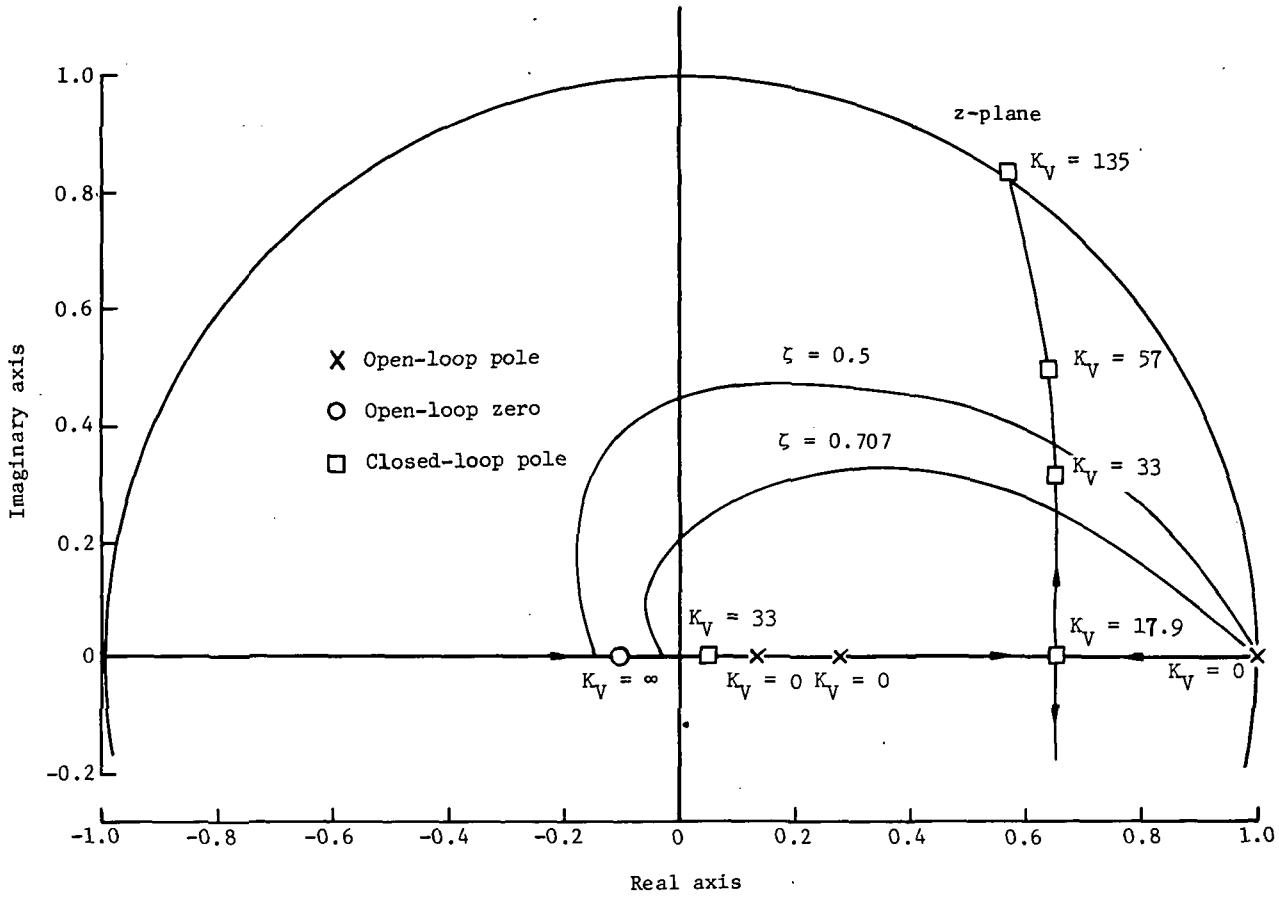

Figure 19.- z-transform root locus for uncompensated system.

compensation was altered to provide additional flexibility through a wider range of possible values of K_V. The compensation was changed to $(s + 8)/(s + 1.1)$, which allowed K_V to be increased by a factor of 4 to 230 per second. The root locus for the final configuration is shown in figure 20 for the characteristic equation

$$1 + KG_2\,G_3(z) = 1 + K\left(6.89 \times 10^{-19}\right)\left[\frac{(z + 0.11)(z + 1.826)}{(z - 0.135)(z - 0.278)}\right.$$

$$\left.\times \frac{(z - 0.923)\left(z + 1.15 \times 10^{11}\right)}{(z - 0.989)(z - 1)}\right] \tag{36a}$$

where

$$K_V = \frac{K}{3520} \tag{36b}$$

The root locus is similar to the one shown in figure 18, except for K_V. At the operating gain of 230 per second, ω_d is approximately 39 radians per second, which is

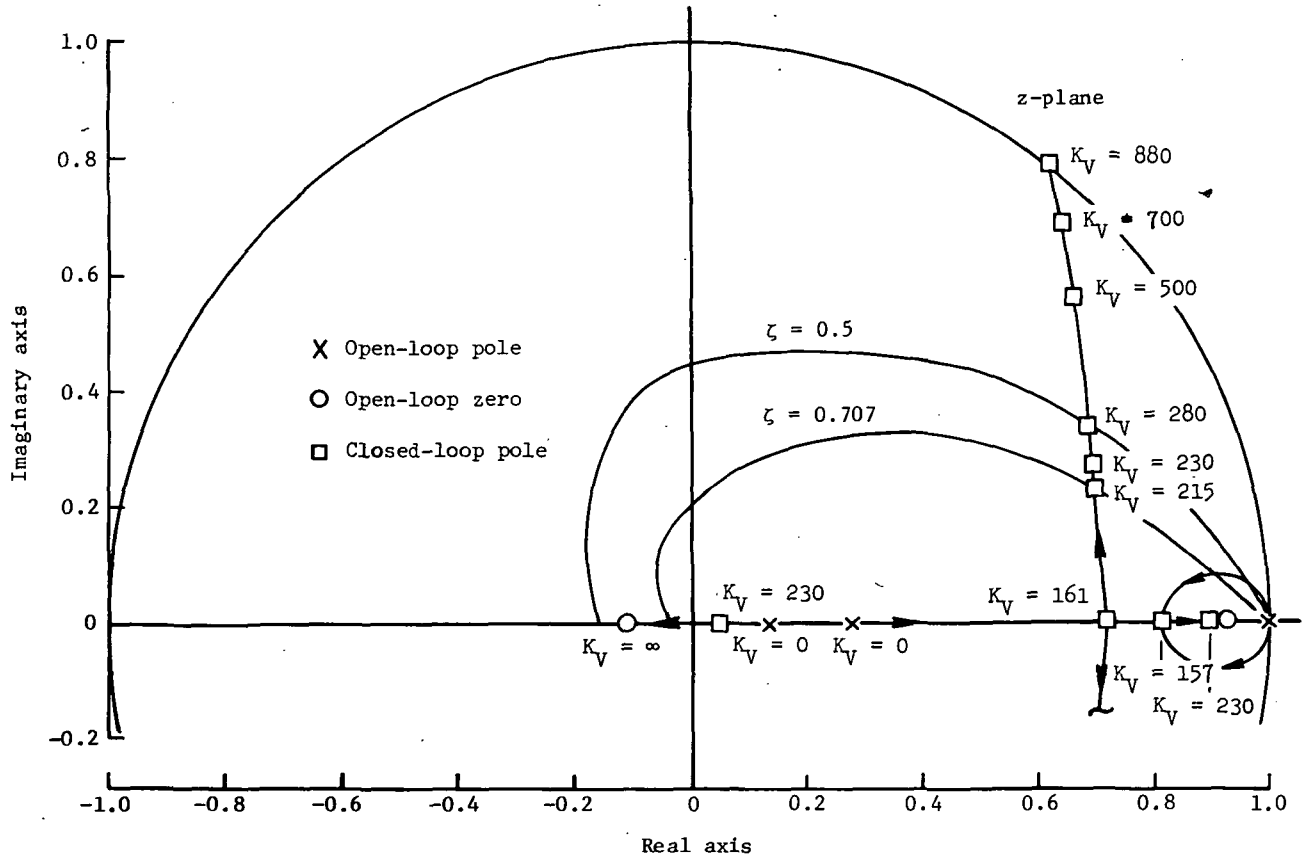

Figure 20.- z-transform root locus for system with (s + 8)/(s + 1.1) compensation.

slightly less than the ω_d of 44 radians per second for the previous compensation. Furthermore, the control system now becomes unstable at a gain of 880 per second. For the operating gain of 230 per second, the gain margin is 3.8, as compared with a gain margin of 4.1 for the previous compensation.

Based upon the root locus shown in figure 20, the control system looks well behaved and very stable. However, the closed-loop transient response and bandwidth need to be investigated. As shown in equation (26a), numerator dynamics may have a significant effect on the closed-loop response. The time-domain response at the sampling instants can be obtained from the inverse z-transform of equation (26a). Other techniques – such as the modified z-transform method – are available to obtain the response between sampling periods. A better method is to use the analog computer because an exact model of the sensor can be simulated and the output is continuous for all periods of time. The next section contains the results of the analog computer analysis for the cases of the two compensators discussed and for cases with and without sensor noise.

ANALOG COMPUTER ANALYSIS

An analog computer simulation is a typical method used to verify and improve system performance. The various component gains and break frequencies determined from the preceding analysis are used in the simulation, which also includes sensor noise. The digital sensor, which had been approximated by a first-order time lag, sampler, and zero-order hold, has been simulated by a combination of electronic switches, integrators, and digital logic modules to approximate more closely the actual hardware.

The operation of the digital sensor has previously been discussed in the section entitled "Component Operation and Mathematical Model." To summarize, a triangular sweep signal scans the electron image across a slit that is centrally located in the electron focal plane. Each time the electron image crosses the slit, an electrical pulse is generated. By counting time between successive pulses, the star image position on the optical focal plane is determined. The electrical pulse generated by the sensor contains noise, which is a function of the guide-star magnitude (ref. 15). The net effect of this noise is a time variation in the detected pulses, thereby causing an error in the position information.

Figure 21 contains a record showing the response of the simulated sensor to a rate input disturbance that is 0.01 times the rate of the sweep signal. The traces shown in

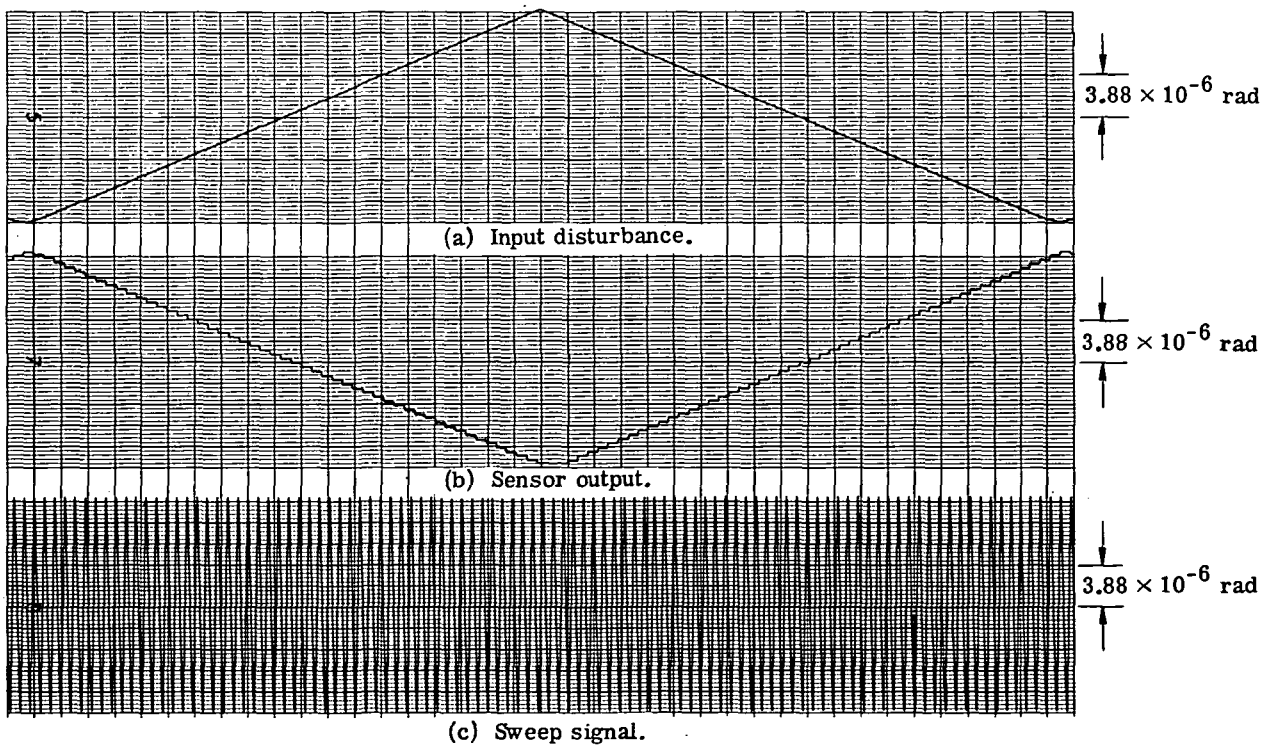

Figure 21.- Computer simulation of sensor response to rate input disturbance.

figures 21(a), 21(b), and 21(c) are the input disturbance, output E_h from the zero-order hold, and the sweep signal, respectively. In the control system, the polarity of E_h is not reversed as shown in the oscillograph record. Figure 22 shows the output signal from the simulated sensor for a constant position +10-magnitude star. As in figure 21, the amplitude is shown in terms of angle rather than voltage. The signal-to-noise ratio was taken from experimental data (ref. 15).

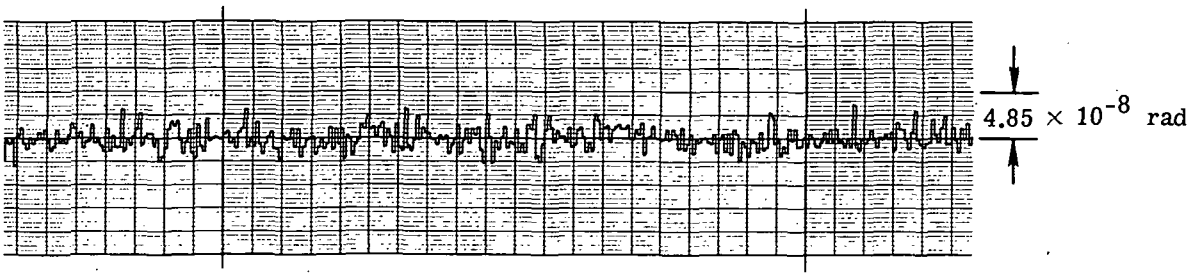

Figure 22.- Computer results for output signal from zero-order hold for stationary +10-magnitude star.

The two compensators $(s + 8)/(s + 4.5)$ and $(s + 8)/(s + 1.1)$ are described in the section entitled "Design Analysis." For $(s + 8)/(s + 4.5)$, the open-loop gain of the control system is 57 per second. By using this gain and the associated compensator, the star image error was measured for the specified rate input disturbance of 0.92×10^{-6} radian per second. The peak star image position error X_e was equivalent to 2.62×10^{-8} radian with no noise, compared with the design value of 1.6×10^{-8} radian, and approximately 4.85×10^{-8} radian when guiding on a +10-magnitude star. The reason that the design factor of 3 (without noise) was not achieved is due to the inherent inaccuracies in mathematically modeling the sensor.

In order to improve system performance, the compensation was changed to $(s + 8)/(s + 1.1)$ and the open-loop gain was increased to 230 per second. Figure 23 contains results for the closed-loop system when the input disturbance is a sine wave of amplitude 0.291×10^{-6} radian and frequency of 0.5 hertz. The record in figures 23(a) to 23(e) includes the input disturbance, mirror position, mirror rate, star image position, and sensor output. The scales for star image position and sensor output have units of angle rather than linear displacement and voltage. For the specified rate input disturbance of 0.92×10^{-6} radian per second, the star image position error was approximately 1.16×10^{-8} radian. Figure 24 shows the same variables for the condition of white noise added to the input disturbance just described. For this case the star image position error was approximately 2.5×10^{-8} radian. Results from another run made with noise as the only disturbance show that the star image position error is approximately 1.07×10^{-8} radian. This error is approximately the same as the error caused by a rate input disturbance and no noise. A comparison of figures 23 and 24 shows that

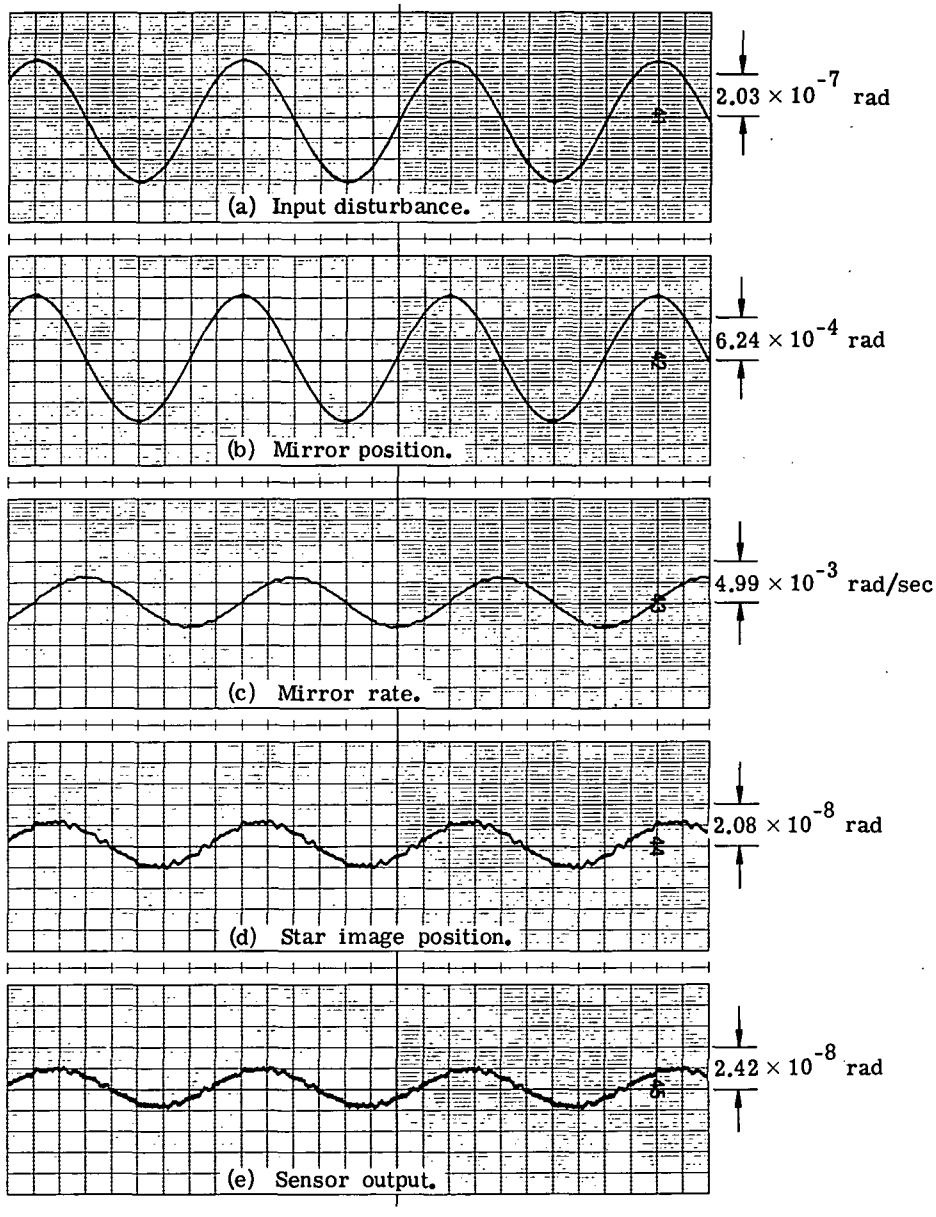

Figure 23.- Computer results of control-system response to sine wave disturbance with frequency of 0.5 hertz and amplitude of 0.06 arc second.

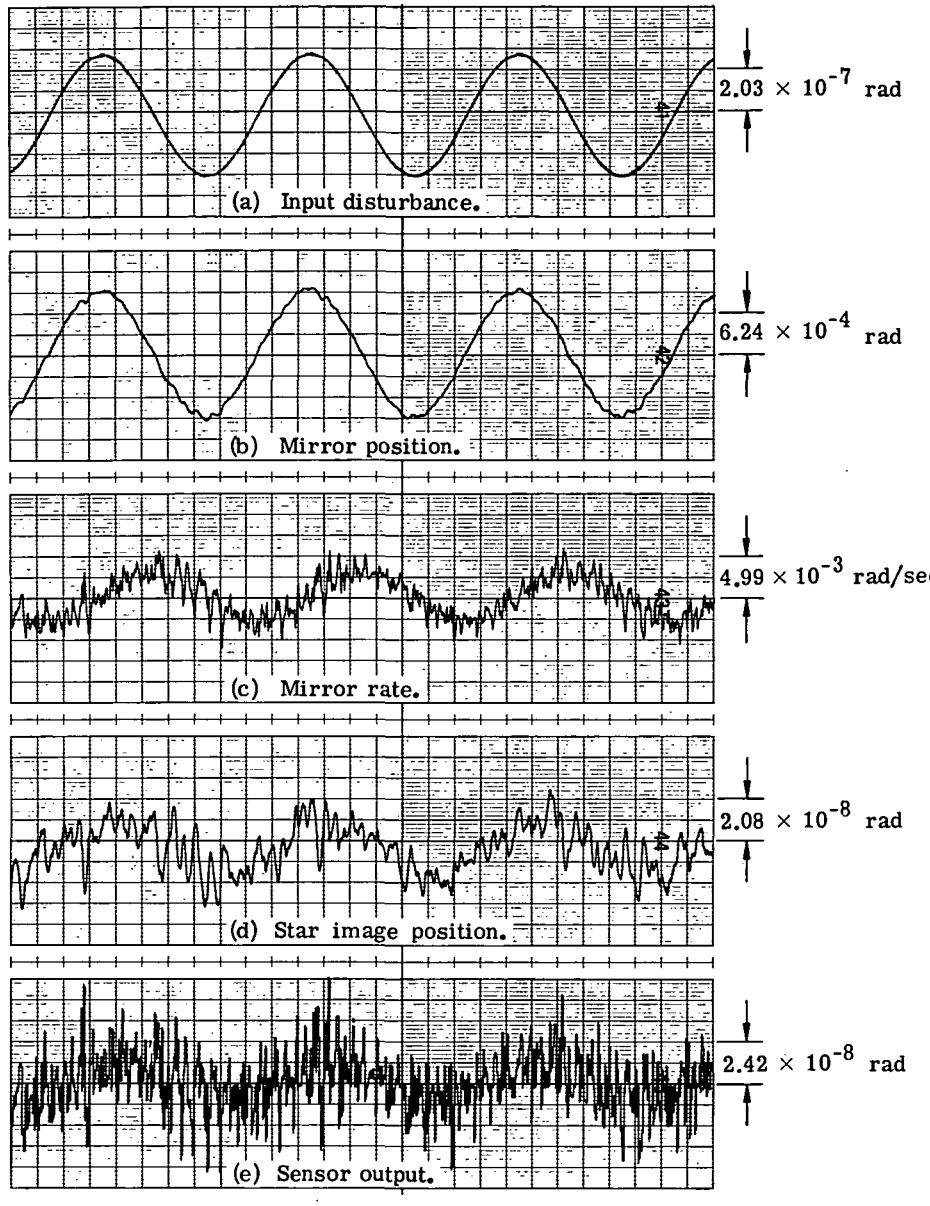

Figure 24.- Computer results of control-system response to +10-magnitude star with sine wave disturbance of 0.5 hertz and amplitude of 0.06 arc second.

the star image position error resulting from noise caused by guiding on a +10-magnitude star is approximately double the error resulting from a noise-free input disturbance. Furthermore, for the specified input disturbance, which has a maximum input of 0.92×10^{-6} radian per second and a star magnitude of +10, the peak star image position error is approximately one-half of the specified maximum error of 4.88×10^{-6} radian.

A frequency-response test for the closed-loop system shows that the bandwidth is 10 hertz and the frequency at the peak amplitude is 5 hertz. The phase shift at the 3-decibel point is approximately 150^{o}. The bandwidth of 10 hertz is within the desired goal of 5 to 10 hertz. Figure 25 shows the control-system response to a step input disturbance. The peak overshoot in mirror position is approximately 36 percent. The system gain was increased to determine the gain that just causes instability. The measured value of 920 per second checks closely with the calculated value of 880 per second (fig. 20).

With the compensation set at $(s + 8)/(s + 1.1)$, the control system meets all design specifications. The position error of 2.5×10^{-8} radian, when following a rate input disturbance of 0.92×10^{-6} radian per second and guiding on a +10-magnitude star, is approximately twice as good as required. The bandwidth of 10 hertz meets the goal of 5 to 10 hertz. The next section describes the hardware results for a bright star and a +10-magnitude star. Various oscillograph records are included for comparison with those obtained in the analog computer simulation.

HARDWARE RESULTS

Various steady-state and dynamic checks have been made on the control system by using the actual hardware that has been described in previous sections. The digital sensor, shown schematically in figure 4, consists of an image dissector tube, a special purpose digital computer, and other associated electronics. At the end of each sampling period, the digital number is shifted to a digital-to-analog converter that also performs the operation of a zero-order hold. The simulated guide star is comprised of a light source and a pinhole aperture. Light from the simulated star is collected by a 3.81-centimeter lens (ref. 15) that has been specially designed to produce a star image that has the exact size and motions on the focal plane of the simulated telescope as it has in a 3-meter-diameter telescope operating at f/100. After passing through the lens, the light rays reflect from the two mirrors of the image motion compensator before being focused on the optical focal plane. A photograph of the image motion compensator is shown in figure 9. Other system components include a torque motor to drive the image motion compensator, a tachometer to generate rate signals, and electronics.

During typical operation, the control system regulates the star image motion to compensate for motions between the simulated star and telescope. Because it is impractical to move either the simulated star or the simulated telescope at the high rates

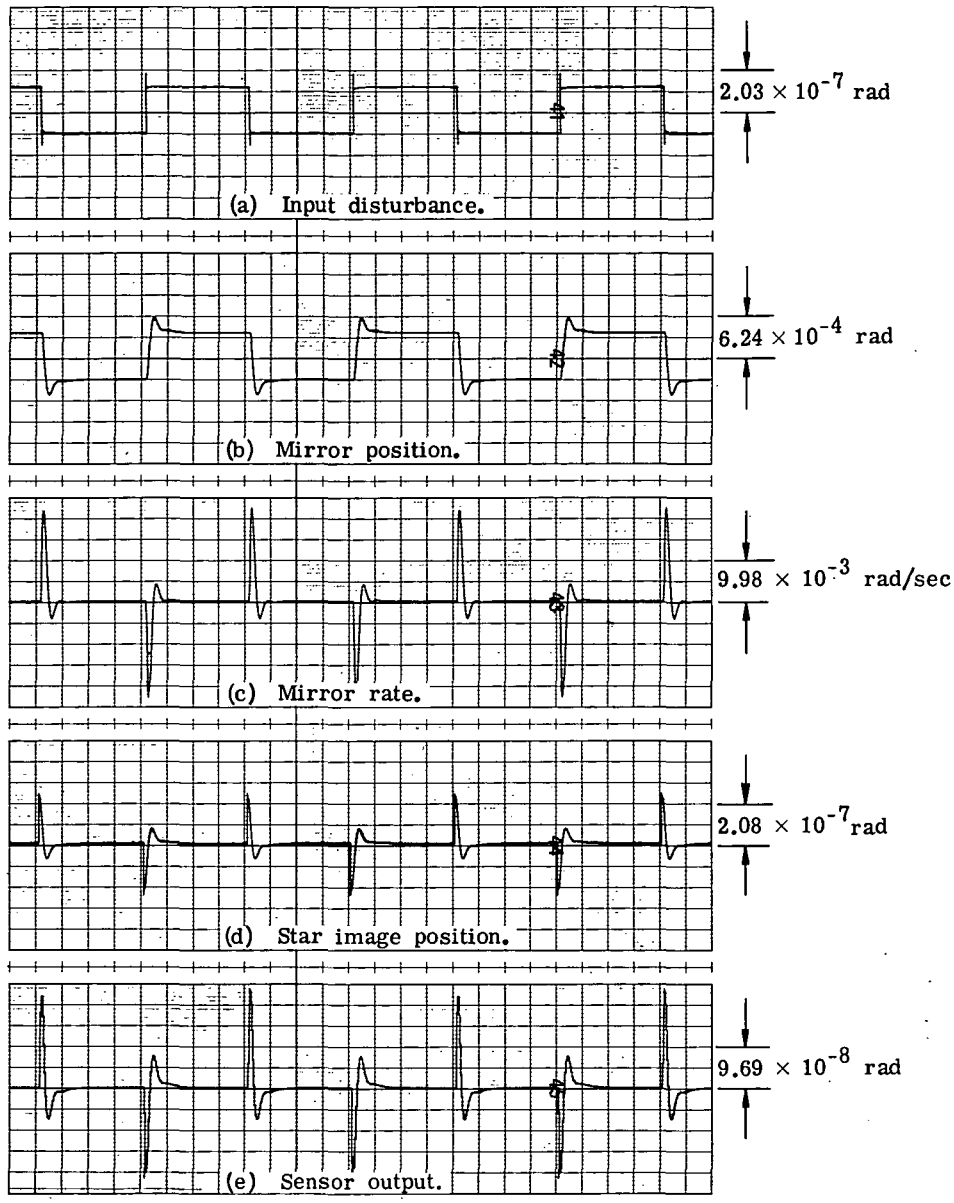

Figure 25.- Computer results of control-system response to step input disturbance with open-loop gain of 230 per second.

required to check adequately the control system, a different technique is employed. The input disturbance is simulated by passing a modulated current through the deflection coils of the tube; the modulated current consists of the reference sweep signal and the dynamic signal.

When the regulating system locks onto the star image and maintains it at approximately a null position, the need for a wide field of view in the digital sensor is diminished. A more important need is the stability of the star image regulating system and the need to minimize the possible loss of the star image because of noise spikes from the sensor. Experimental results show that the signal-to-noise ratio of the digital sensor is a function of the sensor field of view (ref. 15). The reason is that the field of view is directly proportional to the electrical sweep amplitude in the image dissector tube. A decrease in the sweep amplitude causes the star image to cross the slit in the tube at a proportionally slower velocity, thereby increasing the signal-to-noise ratio. For example, decreasing the sensor field of view by a factor of 2 allows the signal-to-noise ratio to be increased by a factor of 1.4. The net effect of increasing the signal-to-noise ratio is the same as using a brighter guide star. Note that although the sensor field of view is decreased, the total usable field of view of the fine-pointing system is maintained because of the range of the image motion compensator.

An adaptive control technique is used to obtain this improved characteristic of the digital sensor. A decrease in the field of view of the sensor causes a corresponding percentage increase in the sensor gain K_S and a similar decrease in the bandwidth of the sensor output signal pulses (fig. 4(c)). In order to compensate for this change in bandwidth, the bandpass filter internal to the sensor electronics must be changed proportionally to insure proper signal conditioning. This change should have no effect on the dynamic response of the control system. In contrast, the control loop must compensate for the increased sensor gain. The approach used is to decrease the gain of compensation K_C (fig. 15), thereby maintaining the total-loop gain constant. When the star image regulating system is used in the dual-level control mode, the gain and filter switchings are controlled automatically through a computer as a function of the star image position X_e, mirror position α, and mirror rate. For the purpose of demonstration, the results shown in this paper were obtained by manually switching the field of view, filter bandpass, and compensator gain simultaneously.

Typical dynamic checks include system response to a step input disturbance and various rate inputs, and a system frequency response utilizing a bright star (+7.85 magnitude) and a +10-magnitude star. The gain constants for the nominal case are shown in table 3 and refer to the block diagram in figure 15. Several individual gains are different from those used in the analog simulation; however, the control-system open-loop gain and break frequencies remain unchanged.

TABLE 3.- NOMINAL GAIN CONSTANTS

K_f, m/rad	305
K_s, $\frac{\text{V-sec}}{\text{m}}$	676 000
K_c, V/V	0.0815
K_a, V/V	1000
K_t, N-m/A	0.593
R, ohms	10
B, $\frac{\text{N-m-sec}}{\text{rad}}$	0.0344
J_L, $\frac{\text{N-m-sec}^2}{\text{rad}}$	0.0141
K_m, m/rad	0.1015
K_r, $\frac{\text{V-sec}}{\text{rad}}$	0.03
n	4
T, sec	0.01

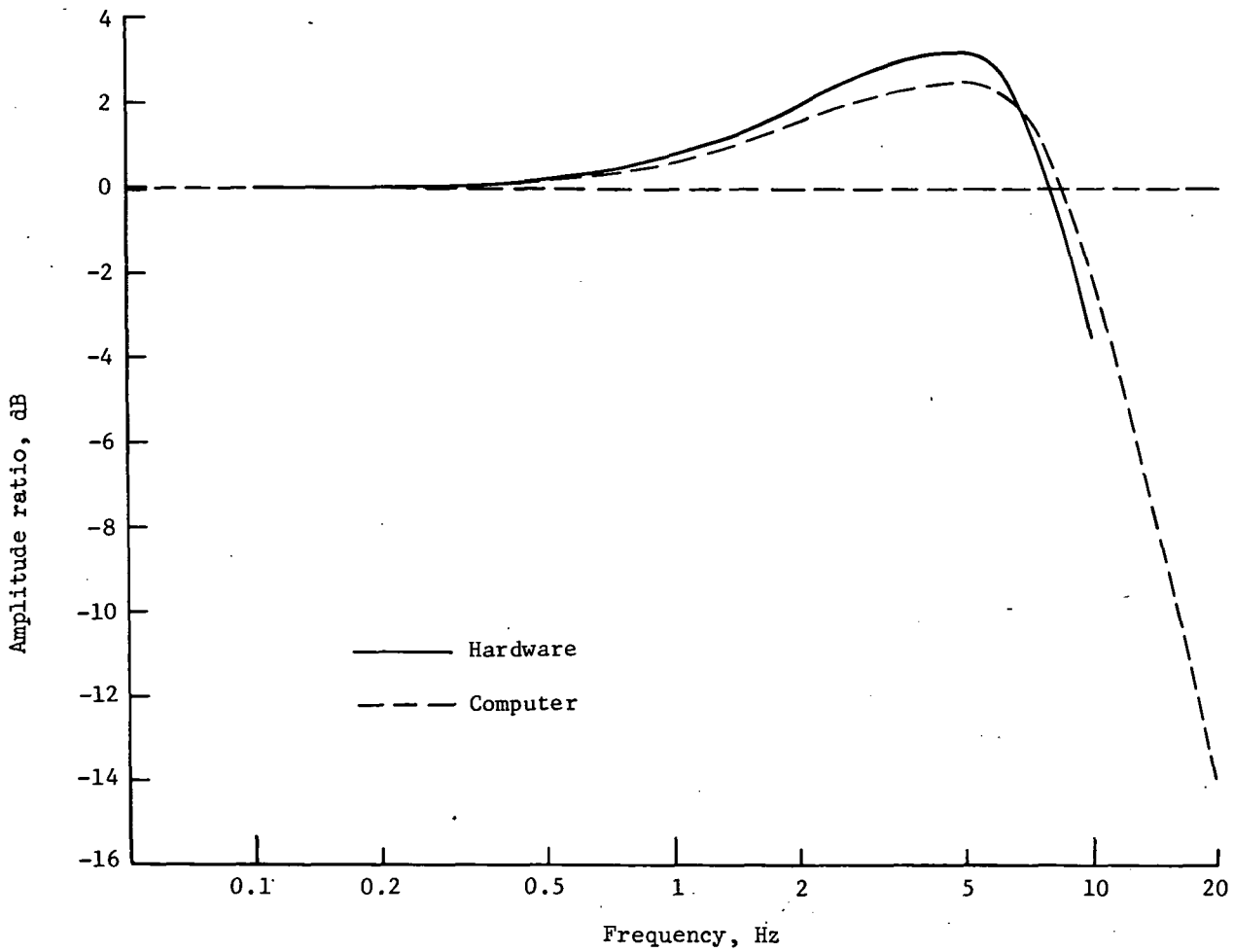

Figure 26.- Frequency response of control system for hardware and computer simulation.

The dynamical response of the system was measured while guiding on a +7.85-magnitude star. Although this star is relatively bright, the sensor noise prohibits an exact measurement of star image position. One typical performance check on a control system is a frequency response. A sine wave input disturbance of approximately 2.91×10^{-7}-radian amplitude was simulated over a frequency range of 0.1 to 10 hertz. A plot of the amplitude ratio as a function of frequency for the hardware and the analog computer simulation is shown in figure 26. The frequency at the peak amplitude for both cases is approximately 5 hertz and the bandwidth, approximately 10 hertz. The peak amplitude is approximately 10 percent higher for the hardware than that obtained on the computer. Figure 27 shows the response of several system variables to a step input disturbance of 4.85×10^{-8} radian. The record contains mirror position, mirror rate, and sensor output as measured at the zero-order hold. The mirror-position overshoot of 40 percent compares favorably with the 36-percent overshoot measured on the computer (fig. 25). The rate transducer shows 60-hertz pickup noise, which is not present in the actual system.

One practical difficulty in utilizing the sensor hardware is the inability to measure directly the star image position on the focal plane. The digital sensor output contains noise which tends to obscure the oscillograph recording containing the actual star image position. This difficulty can be minimized by passing the sensor output through a low-pass filter before recording it. Figure 28 shows results of an unfiltered sensor output and with low-pass filters of 10, 5, and 1 hertz. The rate input disturbance is shown for positive and negative going rates of 0.92×10^{-6} radian per second. The unfiltered sensor output has many noise spikes greater than the desired goal of 4.85×10^{-8} radian; whereas the trace for the 10-hertz low-pass filter shows the star image position to be within specification. Because the control system has a 10-hertz bandwidth, this record should approximate the actual star image position. The results for the 5-hertz low-pass filter are approximately twice as good as the previous case. The steady-state position error can be determined from the trace for the 1-hertz low-pass filter because most of the noise has been eliminated. Results show that the steady-state position error is approximately 10 times better than the required goal of 4.85×10^{-8} radian; this checks closely with the design safety factor of 12. There are a few exceptionally high noise spikes in all of the records. Because of the dim guide star and high-sweep frequency of the star sensor, star detection signal pulses may be missed or noise spikes may be detected in place of an actual signal pulse. The net result is an incorrectly measured star image position. Note that the mirror position (fig. 28(f)) is still a relatively smooth curve. Electronic techniques which can reduce the possibility of these noise spikes are available.

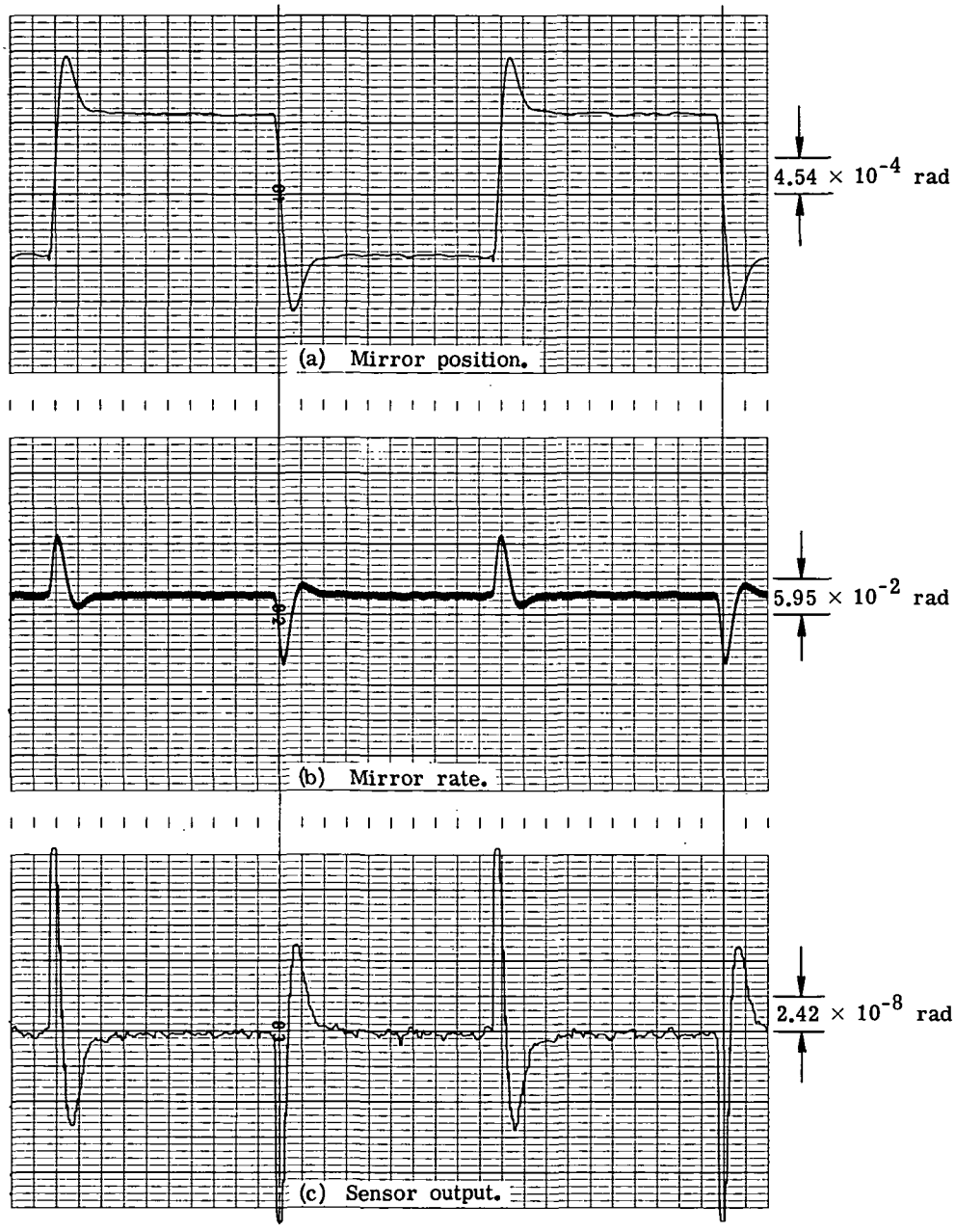

Figure 27.- Control-system response to step input disturbance using hardware.

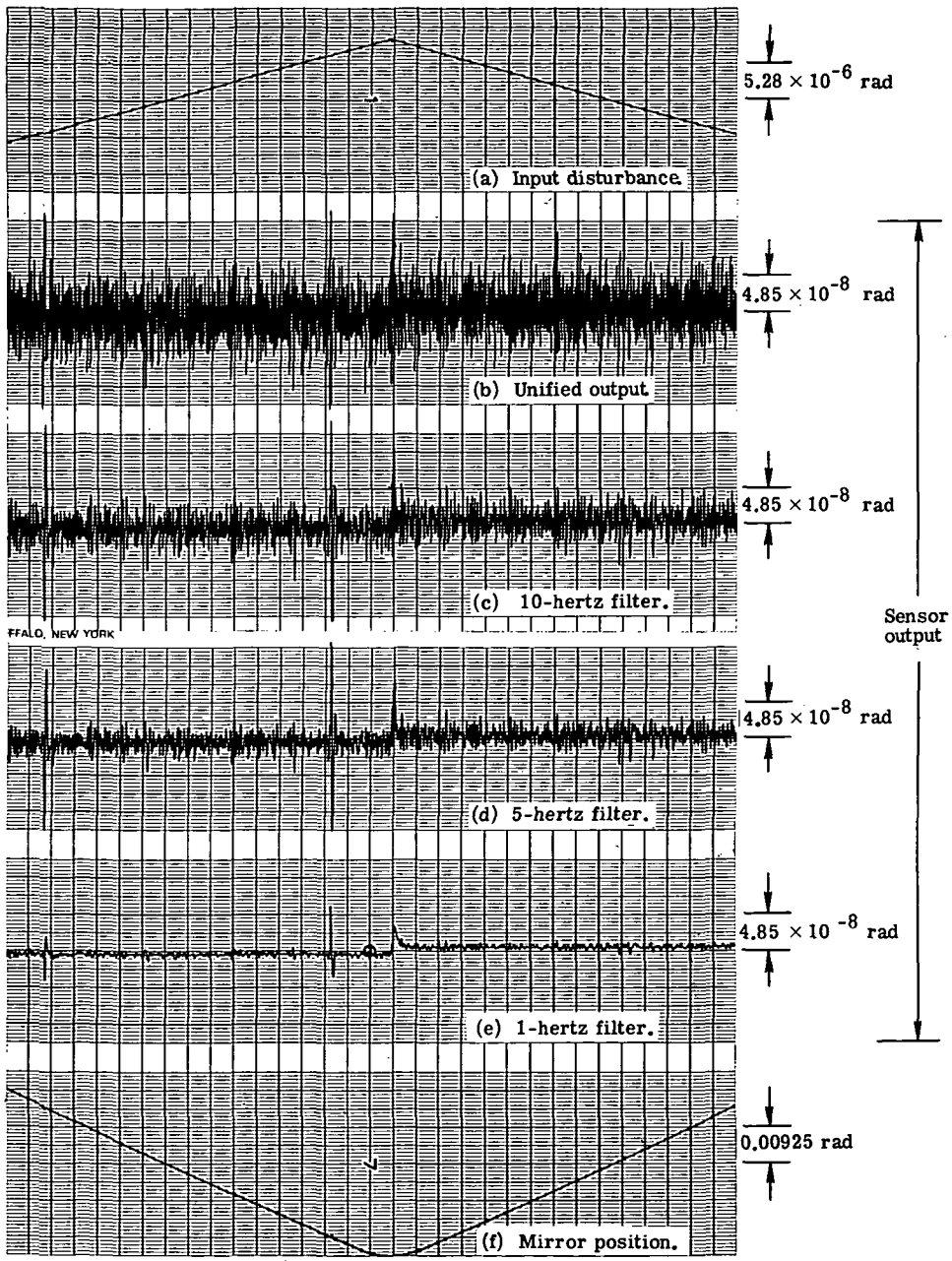

Figure 28.- Sensor output with filters of 10, 5, and 1 hertz.

One technique of measuring system error is to maintain zero input disturbance and observe the mirror position as a function of sensor noise (fig. 29). For this condition, the mirror position is an actual measure of star image position. A mirror rotation of 1.455×10^{-4} radian corresponds to a star image error of 4.85×10^{-8} radian. Despite the fact that the star sensor shows the star image position out of tolerance, the mirror position is just within the required limits. Experimental results for the image dissector tube used in this control loop show that the signal-to-noise ratio is approximately 1.5 times worse than the ratio that was obtained from tests of a previously used image dissector

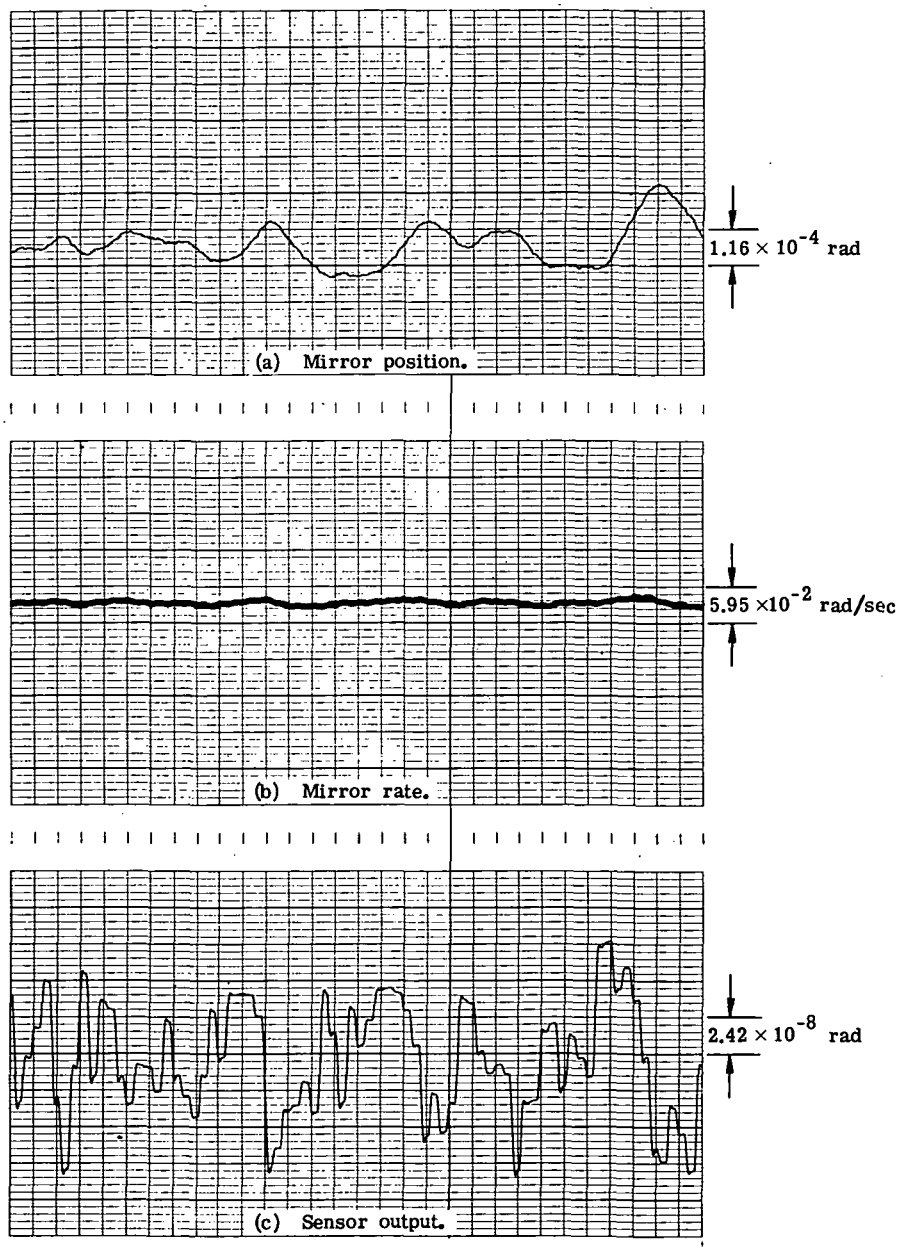

Figure 29.- System response to noise excitation using hardware.

(ref. 15) and simulated on the analog computer. In order to measure the effect of the adaptive control technique, the sensor field of view was decreased by a factor of 8, thereby increasing the sensor signal-to-noise ratio by a factor of 2.8 (ref. 15). For this condition, the mirror position is maintained within 0.55×10^{-4} radian, which is reasonably close to the predicted value (fig. 30). The sensor output also shows a substantial improvement in signal-to-noise ratio and indicates a star image position error within the desired goal.

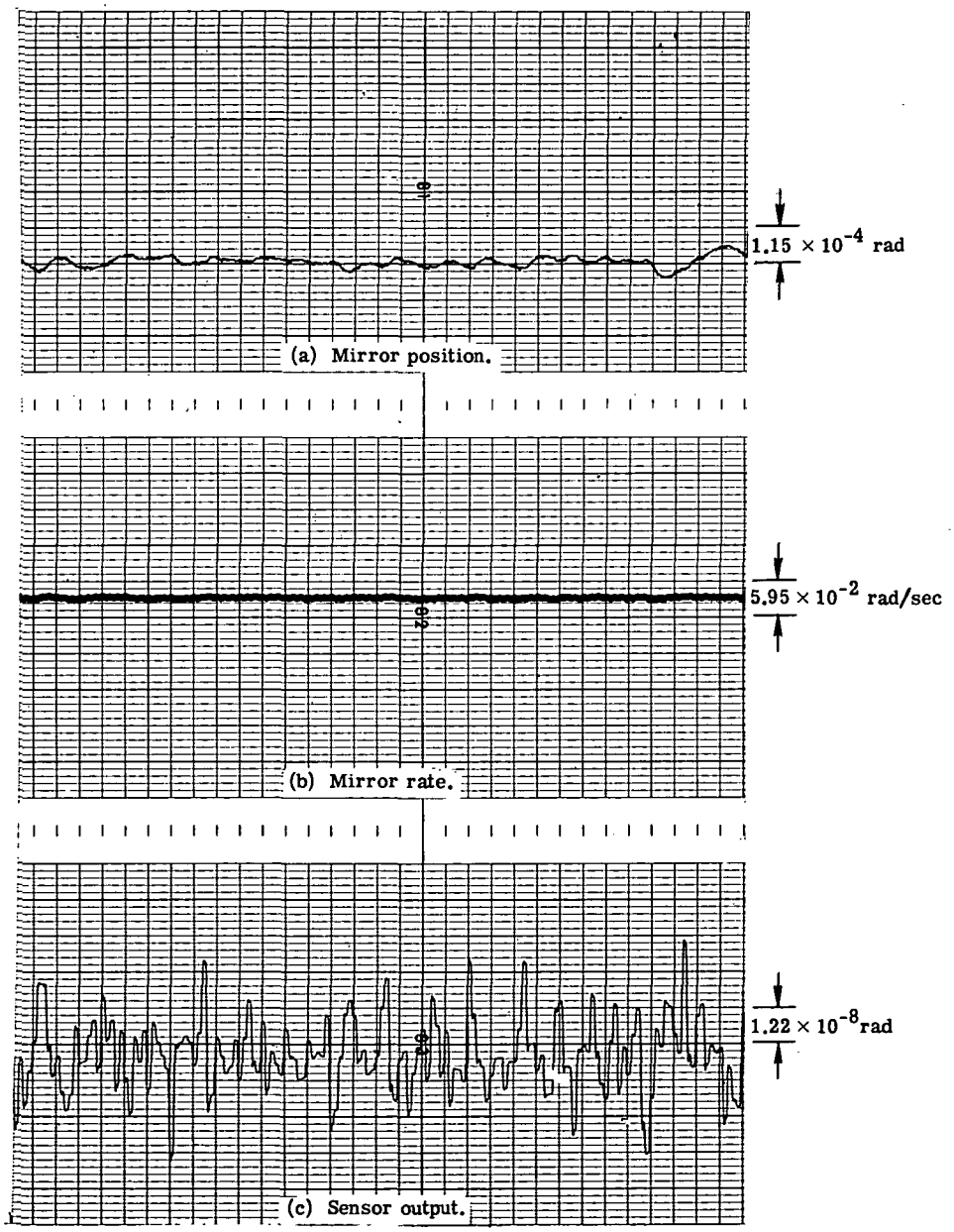

Figure 30.- System response to excitation using adaptive control technique.

Similar improved results for the adaptive control system are observed by comparing figures 31 and 32, which show system response to a sine wave disturbance of 0.5-hertz frequency and 0.291×10^{-6}-radian amplitude. Figure 31 is for the nominal case; whereas figure 32 is for the adaptive control system. The effect of sensor noise on mirror position is shown to be decreased for the adaptive control system. Furthermore, for this case, the peak noise at the sensor output is approximately half the amplitude as it is for the nominal case. Another test for a step input disturbance shows results very similar to those in figure 27 for the nominal case.

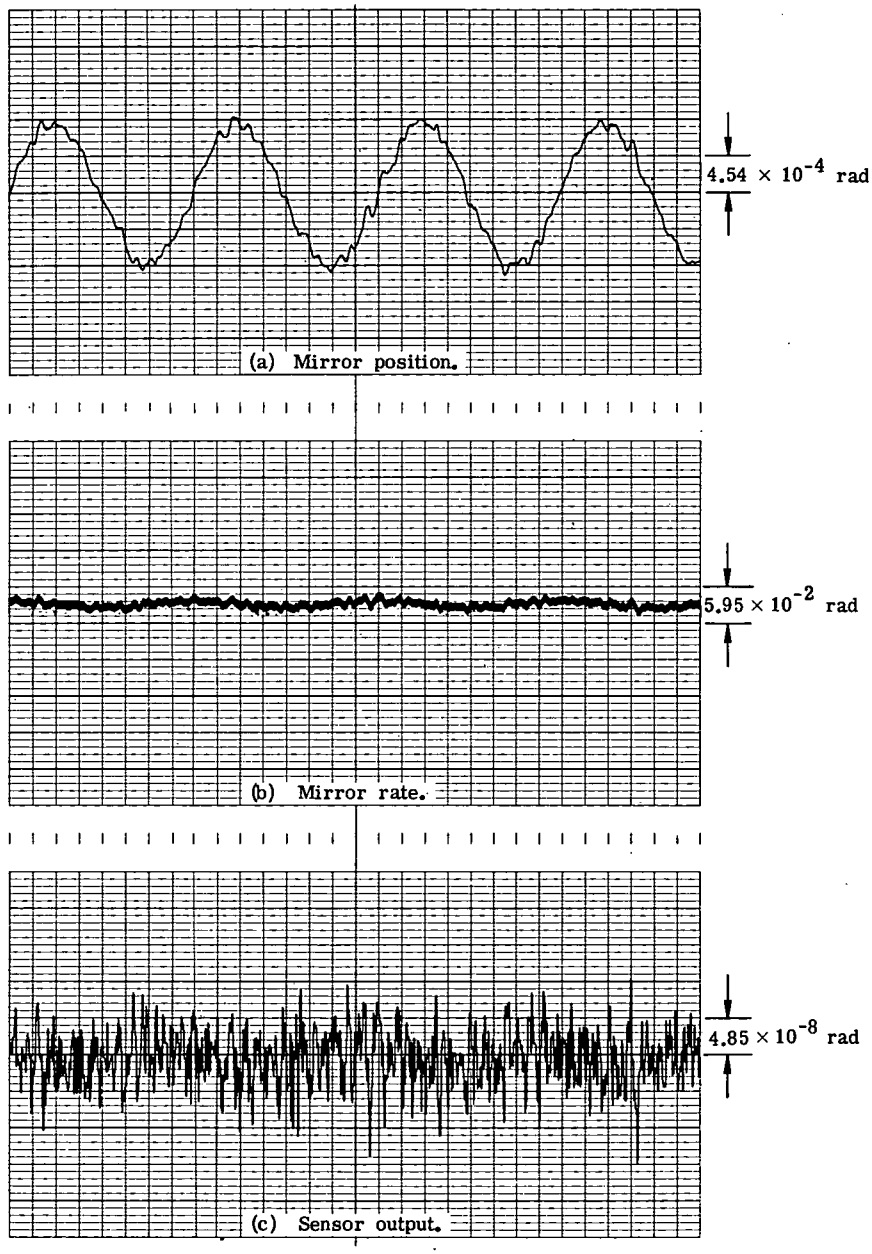

Figure 31.- System response to sine wave disturbance of 0.5-hertz frequency and 0.06-arc-second amplitude using hardware.

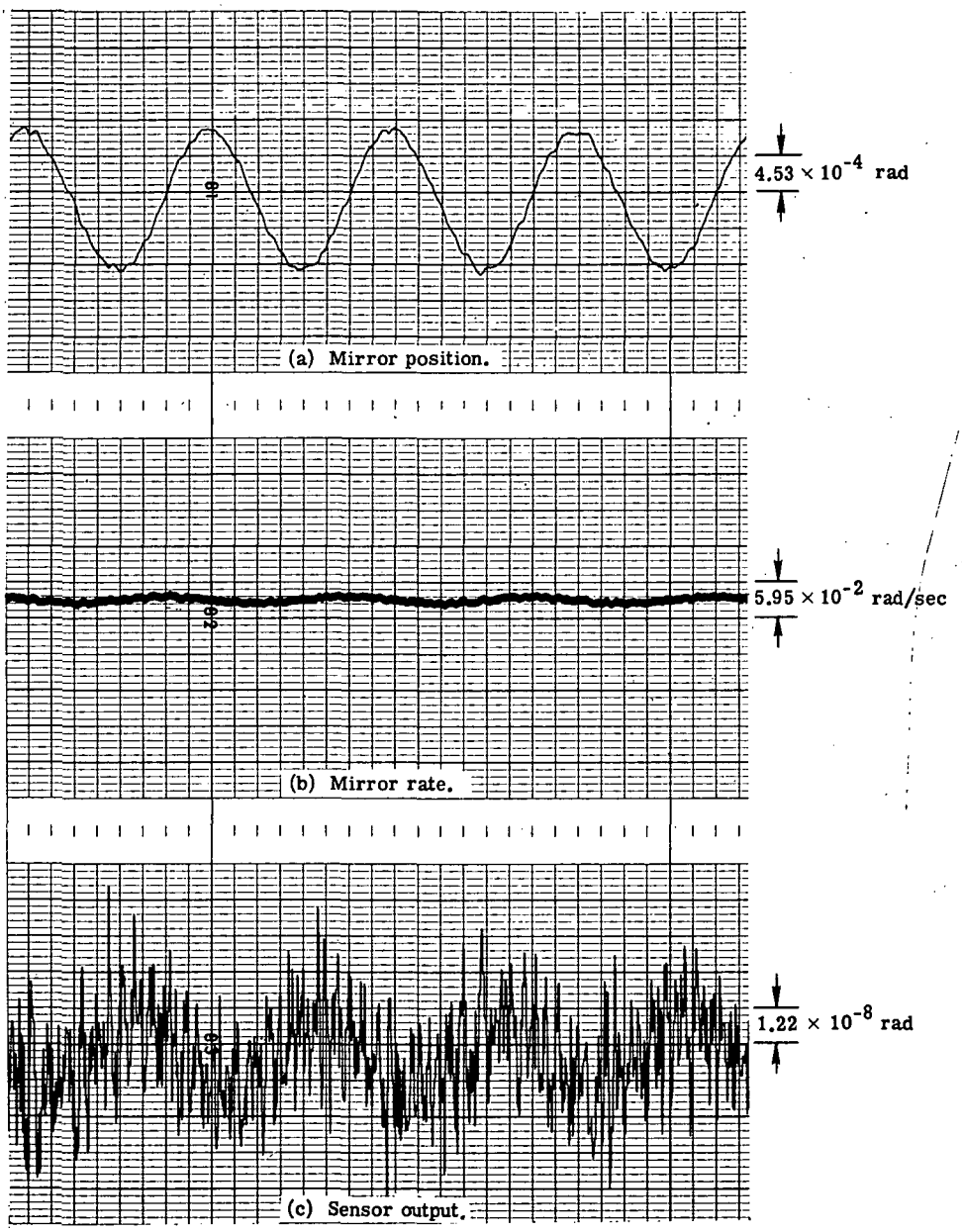

Figure 32.- System response to sine wave disturbance of 0.5-hertz frequency and 0.291×10^{-6}-radian amplitude using adaptive control technique.

The results for the adaptive control system demonstrate that by decreasing the sensor field of view and maintaining the mirror control range constant, the star image position error is decreased by approximately the square root of the change in the field of view. As shown in figure 29, the mirror position, representing the star image position error, for the nominal case is approximately at the required limit of 1.46×10^{-4} radian as compared with an error of approximately 0.55×10^{-4} radian (fig. 30) when the digital sensor field of view is eight times smaller. Dynamically, system response is approximately the same for both cases.

CONCLUDING REMARKS

The feasibility of operating a star image regulating system for a representative telescope within the stability limits of a coarse-pointing control system is demonstrated. The use of dual-level control permits utilization of a high bandwidth control system without the likelihood of exciting structural vibrations in the telescope and minimizes the stringent pointing requirements of the primary control system. The ingredients of the fine-pointing control system include a digital star sensor, an optical star image motion compensator, a controller, and compensation.

The heart of the digital sensor is an image dissector tube that operates with a triangular sweep frequency. The peak amplitude of the sweep signal must be large enough to cover the complete field of view of the fine-pointing system. Mathematical analysis has shown that the steady-state error to a position input is zero (assuming no noise); whereas the digital sensor follows a velocity input with a constant-position error. Furthermore, this position error is approximately proportional to the velocity of the star image across the focal plane. For a given sweep amplitude and a worst case velocity input disturbance, the position error is directly related to the sampling period. The digital sensor is modeled as a first-order lag equal to one-half the sampling period followed by a sampler and a zero-order hold.

The advantage of the optical star image motion compensator over other techniques includes the ability to control two or more star images simultaneously in two axes with only two plane reflecting mirrors. Analysis has shown that the star image displacement along the optical focal plane is a function of the distance between the two mirrors and the mirror rotation angle. For small angles, the mathematical model of the image motion compensator is approximated by a pure gain constant.

In order to make the regulating system design specific, realistic performance specifications have been selected for a representative telescope. In particular, for a specified sine wave input disturbance of 2.91×10^{-7}-radian amplitude and 0.5-hertz frequency, the control system regulates the star image position within the desired goal of

4.85×10^{-8} radian while guiding on a simulated +10-magnitude star. Furthermore, the measured bandwidth of 10 hertz is within the desired range of 5 to 10 hertz.

By using adaptive control techniques, the star image position error is shown to be decreased by approximately the square root of the decrease in the sensor field of view. Dynamically, system response is approximately the same as for the nominal case. The controllable range of the star image motion compensator remains unchanged as the sensor field of view is varied.

An approximate continuous-data network that was used to establish system break points and develop compensation is justified by the good performance characteristics attained from the subsequent z-transform analysis and hardware checks. Measured system responses of the analog computer simulation and the actual system components to sinusoidal and step input disturbances show close agreement. Although within the desired goal, the steady-state accuracy of the actual system is slightly degraded from the accuracy measured on the analog computer because of the additional noise generated by the star sensor. While no attempt was made to optimize system performance, the desired goals were attained in a relatively straightforward manner.

Langley Research Center,
National Aeronautics and Space Administration,
Hampton, Va., April 13, 1973.

APPENDIX A

DERIVATION OF MATHEMATICAL MODEL FOR STAR SENSOR

In this appendix, a mathematical model is developed for the star sensor by first deriving an expression for the attitude-measurement error of a star image moving with constant velocity and then deriving an equation for the time constant used in the model. Representative waveforms for the star images moving with constant position and constant velocity are shown in figure 5.

For the steady-state case, the star sensor measured output N_1 is defined as

$$N_1 = t_2 - t_1 \tag{A1}$$

where t_1 is the time between the first and second pulses and t_2 is the time between the second and third pulses. For the constant-velocity case, the star sensor measured output N_1' is

$$N_1' = t_2' - t_1' \tag{A2}$$

where the prime (') represents the dynamic condition. For both cases, the position error is computed at time t_b when the amplitude is X_b. Hence, the measurement should be the same in both cases. The difference between equations (A1) and (A2) is the difference in the numbers ΔN_1 as

$$\Delta N_1 = N_1 - N_1' = \Delta t_a + 2\Delta t_b \tag{A3}$$

because

$$t_1' = t_1 + \Delta t_a + \Delta t_b \tag{A4}$$

and

$$t_2' = t_2 - \Delta t_b \tag{A5}$$

because N_1 is exact. The time intervals Δt_a and Δt_b are related to the period T of the sweep signal, the slope m_s of the sweep signal, and the slope m_d of the star image for the dynamic case as

$$\Delta t_a = t_b - T \tag{A6}$$

and

$$\Delta t_b = \Delta t_a + t_c - \frac{T}{2} \tag{A7}$$

Equating the displacements of the sweep signal and star image at times t_c and t_b leads to

$$t_b = \frac{4X_a}{m_s - m_d} \tag{A8}$$

and

$$t_c = \frac{2X_a}{m_s + m_d} \tag{A9}$$

where t_b and t_c are detection times as shown in figure 5 and X_a is the peak amplitude of the sweep signal. By defining

$$R_m = \frac{m_s}{m_d} \tag{A10}$$

where R_m is the ratio of the time rate of change of the sweep signal to the time rate of change of the star image position on the focal plane, the measurement error can be found by substituting equations (A6) to (A10) into equation (A3) as

$$\Delta N_1 = 2T \frac{R_m + 2}{R_m^2 - 1} \tag{A11}$$

The measurement error in equation (A11) is in terms of time and should be converted to a displacement that is equivalent to position error. The following derivation shows that the peak amplitude X_a can be substituted for the period T to obtain this conversion. Detection times t_a, t_b, and t_d are determined from figure 5 as

$$t_a = \frac{X_b}{m_s} \tag{A12}$$

$$t_d = \frac{T}{2} - \frac{X_b}{m_s} \tag{A13}$$

and

$$t_b = T + \frac{X_b}{m_s} \tag{A14}$$

By using equations (A12) to (A14)

$$t_1 = t_d - t_a = \frac{T}{2} - \frac{2X_b}{m_s} \tag{A15}$$

and

$$t_2 = t_b - t_d = \frac{T}{2} + \frac{2X_b}{m_s} \tag{A16}$$

From equations (A1), (A15), and (A16)

$$N_1 = t_2 - t_1 = \frac{4X_b}{m_s} \tag{A17}$$

By rearranging equation (A17)

$$X_b = \frac{N_1 m_s}{4} \cdot \frac{X_a}{X_a} \tag{A18}$$

because

$$T = \frac{4X_a}{m_s} \tag{A19}$$

and then

$$X_b = \frac{N_1 X_a}{T} \tag{A20}$$

Thus, corresponding to equation (A20), the error in the amplitude calculation ΔX_b is proportional to the error in the measured number ΔN_1, as

$$\Delta X_b = \frac{\Delta N_1 X_a}{T} \tag{A21}$$

where ΔN_1 was previously defined in equation (A3). Substitution of equation (A11) into equation (A21) yields

$$\Delta X_b = 2X_a \frac{R_m + 2}{R_m^2 - 1} \tag{A22}$$

which can be approximated as

$$\Delta X_b \approx \frac{2X_a}{R_m} \qquad \left(R_m >> 2; \quad R_m^2 >> 1\right) \tag{A23}$$

Equation (A23) represents the error in the position measurement for the constant-rate star image. For a given X_2, the measurement error can be kept to an acceptable level by selecting the ratio R_m. Because the sensor output follows a rate input disturbance m_d with a constant-position error, the dynamic properties of the sensor can be modeled by a first-order time lag τ, as shown in figure 6, the time constant is related to the position measurement error and slope of the input disturbance as

$$\tau = \frac{\Delta X_b}{m_d} \tag{A24}$$

and by substituting equations (A10), (A19), and (A23) into equation (A24) yields

$$\tau = \frac{T}{2} \tag{A25}$$

which relates the time constant to the sweep period of the star sensor.

To summarize, the derivation of the sensor characteristics utilized star image position. The computations are arranged to produce an estimate of the star image position at every odd-numbered pulse, with the use of that pulse and two previous pulses. For a star with constant position, the position information is available at the sensor output at regular intervals of T. For a time-varying star image, there is a slight nonuniformity in the rate of information from the position sensor. Because the sampling period variation is small, it is assured negligible for the purpose of design. The digital sensor is modeled as the previously described first-order lag followed by a zero-order hold, which is built into the computer. The time constant of the sensor can be varied by adjusting the sampling period T.

APPENDIX B

DERIVATION OF CHARACTERISTIC EQUATION AND APPLICATION OF FINAL-VALUE THEOREM TO CONTROL SYSTEM

A block diagram representing the sampled-data control system is shown in figure 15. The star image position X_e is related to the input disturbance ϕ and the output X_p as

$$X_e(s) = K_f\phi(s) - X_p(s) \tag{B1}$$

and the continuous output of the sensor is

$$E_s(s) = G_2(s)\, X_e(s) \tag{B2}$$

where G_2 is the transfer function of the sensor. The output X_p is related to the sampled data signal E_s^* as

$$X_p = KG_3(s)\, E_s^*(s) \tag{B3}$$

where

$$G_3(s) = G_{ho}(s)\, G_c(s)\, G_1(s) \tag{B4}$$

and K is the gain constant for the complete system. Substitution of equations (B1) and (B3) into equation (B2) yields

$$E_s(s) = K_f\phi(s)\, G_2(s) - KE_s^*(s)\, G_2(s)\, G_3(s) \tag{B5}$$

By taking the pulse transform of equation (B5)

$$E_s^*(s) = \frac{\left[K_f\phi(s)\, G_2(s)\right]^*}{1 + \left[KG_2(s)\, G_3(s)\right]} \tag{B6}$$

By substituting equation (B6) into equation (B3) and taking the pulse transform, the sampled output becomes

$$X_p^*(s) = \frac{K\left[K_f\phi(s)\, G_2(s)\right]^*\, G_3^*(s)}{1 + \left[KG_2(s)\, G_3(s)\right]^*} \tag{B7}$$

The z-transform of $X_p(t)$ is

$$X_p(z) = \frac{K\left[K_f\phi\ G_2(z)\right] G_3(z)}{1 + KG_2\ G_3(z)} \tag{B8}$$

and the characteristic equation is the denominator of equation (B8) set equal to zero.

The z-transform of the star image position is obtained from equation (B1) as

$$X_e(z) = K_f\ \phi(z) - X_p(z) \tag{B9}$$

where $X_p(z)$ is derived in equation (B8). Each term in equations (B8) and (B9) can be broken down into the system break frequencies as

$$K_f\phi\ G_2(z) = K_f Z\left[\phi(s)\ \frac{1}{s + \omega_4}\right] \tag{B10a}$$

$$K_f\ \phi(z) = K_f Z\left[\phi(s)\right] \tag{B10b}$$

$$G_3(z) = \left(1 - z^{-1}\right) Z\left[\frac{s + \omega_1}{s^2(s + \omega_2)(s + \omega_3)}\right] \tag{B10c}$$

and

$$KG_2\ G_3(z) = K\left(1 - z^{-1}\right) Z\left[\frac{s + \omega_1}{s^2(s + \omega_2)(s + \omega_3)(s + \omega_4)}\right] \tag{B10d}$$

where the ω_i (i = 1, 2, 3, 4) have been defined in the text and the list of symbols.

For a rate input

$$\phi(s) = \frac{\phi_o}{s^2} \tag{B11}$$

equations (B10a) and (B10b) become

$$K_f\phi\ G_2(z) = K_f Z\left[\frac{\phi_o}{s^2(s + \omega_4)}\right] \tag{B12a}$$

and

$$K_f\ \phi(z) = K_f Z\left(\frac{\phi_o}{s^2}\right) \tag{B12b}$$

The z-transform of equations (B10c), (B10d), (B12a), and (B12b) can be found by expanding the terms inside of the brackets by the method of partial fractions. The three z-transforms of interest are obtained from tables (ref. 19) as

$$Z\left(\frac{1}{s^2}\right) = \frac{Tz}{(z-1)^2} \tag{B13a}$$

$$Z\left(\frac{1}{s}\right) = \frac{z}{z-1} \tag{B13b}$$

$$Z\left(\frac{1}{s+\omega_i}\right) = \frac{z}{z - e^{-\omega_i T}} \tag{B13c}$$

where $i = 2, 3, 4$.

The resulting partial fractions in the z-domain are

$$K_f\,\phi(z) = \phi_o K_f \frac{Tz}{(z-1)^2} \tag{B14a}$$

$$KG_2\,G_3(z) = K\left(1 - z^{-1}\right)\left[\frac{C_a Tz}{(z-1)^2} + \frac{C_b z}{z-1} + \frac{C_c z}{z-a} + \frac{C_d z}{z-b} + \frac{C_e z}{z-c}\right] \tag{B14b}$$

$$K_f\phi\,G_2(z) = \phi_o K_f\left[\frac{C_f Tz}{(z-1)^2} + \frac{C_g z}{z-1} + \frac{C_h z}{z-c}\right] \tag{B14c}$$

and

$$G_3(z) = \left(1 - z^{-1}\right)\left[\frac{C_i Tz}{(z-1)^2} + \frac{C_j z}{z-1} + \frac{C_k z}{z-a} + \frac{C_l z}{z-b}\right] \tag{B14d}$$

where

$$a = e^{-\omega_2 T} \tag{B15a}$$

$$b = e^{-\omega_3 T} \tag{B15b}$$

$$c = e^{-\omega_4 T} \tag{B15c}$$

and $C_a, \ldots, C_l$ are the residues. Substitution of equations (B14) and (B15) into equation (B9) yields

$$X_e(z) = \frac{\phi K_f z}{(z-1)^2}\left[\frac{S_o + S_1(z-1) + S_2(z-1)^2 + S_3(z-1)^3 + S_4(z-1)^4}{S_5}\right] \tag{B16}$$

where

$$S_o = KT^2(z-a)(z-b)(z-c)\left(C_a - C_f C_i\right) \tag{B17a}$$

$$S_1 = T(z-a)(z-b)(z-c)\left(1 + KC_b - C_f C_j - C_g C_i\right) \tag{B17b}$$

$$\begin{aligned} S_2 = KT\Big[&C_c(z-b)(z-c) + C_d(z-a)(z-c) + C_e(z-a)(z-b) \\ &- C_f C_k(z-b)(z-c) - C_f C_l(z-a)(z-c) \\ &- \frac{C_g C_j}{T}(z-a)(z-b)(z-c) - C_h C_i(z-a)(z-b)\Big] \end{aligned} \tag{B17c}$$

$$S_3 = K\left[-C_g C_k(z-b)(z-c) - C_g C_l(z-a)(z-c) - C_h C_j(z-a)(z-b)\right] \tag{B17d}$$

$$S_4 = K\left[-C_k C_h(z-b) - C_h C_l(z-a)\right] \tag{B17e}$$

and

$$\begin{aligned} S_5 = (z-1)(z-a)(z-b)(z-c) + K\Big[&C_a T(z-a)(z-b)(z-c) \\ &+ C_b(z-1)(z-a)(z-b)(z-c) + C_c(z-1)^2(z-b)(z-c) \\ &+ C_d(z-1)^2(z-a)(z-c) + C_e(z-1)^2(z-a)(z-b)\Big] \end{aligned} \tag{B17f}$$

The residues $C_a, \ldots, C_l$ are functions of the break frequencies as

$$C_a = \frac{\omega_1}{\omega_2\omega_3\omega_4} \tag{B18a}$$

$$C_b = \frac{\omega_2\omega_3\omega_4 - \omega_1\left(\omega_2\omega_3 + \omega_2\omega_4 + \omega_3\omega_4\right)}{\left(\omega_2\omega_3\omega_4\right)^2} \tag{B18b}$$

$$C_c = \frac{\omega_1 - \omega_2}{(\omega_2)^2(\omega_3 - \omega_2)(\omega_4 - \omega_2)} \tag{B18c}$$

$$C_d = \frac{\omega_1 - \omega_3}{(\omega_3)^2(\omega_2 - \omega_3)(\omega_4 - \omega_3)} \tag{B18d}$$

$$C_e = \frac{\omega_1 - \omega_4}{(\omega_4)^2(\omega_2 - \omega_4)(\omega_3 - \omega_4)} \tag{B18e}$$

$$C_f = \frac{1}{\omega_4} \tag{B18f}$$

$$C_g = \frac{-1}{(\omega_4)^2} \tag{B18g}$$

$$C_h = \frac{1}{(\omega_4)^2} \tag{B18h}$$

$$C_i = \frac{\omega_1}{\omega_2\omega_3} \tag{B18i}$$

$$C_j = \frac{\omega_2\omega_3 - \omega_1(\omega_2 + \omega_3)}{(\omega_2\omega_3)^2} \tag{B18j}$$

$$C_k = \frac{\omega_1 - \omega_2}{(\omega_2)^2(\omega_3 - \omega_2)} \tag{B18k}$$

$$C_l = \frac{\omega_1 - \omega_3}{(\omega_3)^2(\omega_2 - \omega_3)} \tag{B18l}$$

Because the coefficients

$$C_a = C_f C_i \tag{B19a}$$

and

$$C_b = C_f C_j + C_g C_i \tag{B19b}$$

the terms S_0 and S_1 become

$$S_0 = 0 \tag{B20a}$$

$$S_1 = T(z - a)(z - b)(z - c) \tag{B20b}$$

From the final-value theorem for z-transforms (ref. 19)

$$\lim_{t\to\infty} X_e^*(t) = \lim_{z\to 1}\left(1 - z^{-1}\right)X_e(z) \tag{B21}$$

provided that $\left(1 - z^{-1}\right)X_e(z)$ has no poles on or outside the unit circle in the z-plane. Substitution of equation (B16) into equation (B21) yields

$$\lim_{z\to 1}\left(1 - z^{-1}\right)X_e(z) = \lim_{z\to 1}\frac{\phi_o K_f}{z - 1}\frac{\left[S_1(z - 1) + S_2(z - 1)^2 + S_3(z - 1)^3 + S_4(z - 1)^4\right]}{S_5} \tag{B22}$$

and by substituting equations (B17) and (B19) into equation (B22) and making use of equation (B14b)

$$\lim_{z\to 1}\left(1 - z^{-1}\right)X_e(z) = \lim_{z\to 1}\frac{\phi_o K_f}{\frac{1}{T}(z - 1)KG_2\, G_3(z)} \tag{B23}$$

By defining

$$K_V = \frac{1}{T}\lim_{z\to 1}(z - 1)KG_2\, G_3(z) \tag{B24}$$

equation (B23) becomes

$$\lim_{z\to 1}\left(1 - z^{-1}\right)X_e(z) = \frac{\phi_o K_f}{K_V} \tag{B25}$$

Equation (B25) shows that the control system shown in figure 15 follows a rate input with a steady-state position error; the magnitude of the error is proportional to the magnitude of the angular-velocity input.

REFERENCES

1. Wissinger, Alan B.: Large Telescope Experiment Program (LTEP). Vol. I, Pts. 1 and 2. Rep. No. 9800 (Contract NAS 8-21497), Optical Group, Perkin-Elmer Corp., Apr. 24, 1970. (Available as NASA CR-102768 and NASA CR-102769.)

2. Joint Space Panels: The Space Program in the Post-Apollo Period – A Report of the President's Science Advisory Committee. U.S. Govt. Printing Office, Feb. 1967.

3. Frederick, Laurence W., ed.: Applications in Astronomy Suitable for Study by Means of Manned Orbiting Observatories and Related Instrumentation and Operational Requirements. Vols. I and II. NASA Grant No. NsG-480, Leander McCormick Observatory, Univ. of Virginia, 1963. (Available as NASA CR-52897 and NASA CR-112285.)

4. Anon.: Feasibility Study of a 120-Inch Orbiting Astronomical Telescope. AE-1148 (Contract NAS 1-1305-18), J. W. Fecker Div., Amer. Optical Co., [1963]. (Available as NASA CR-66001.)

5. Anon.: A System Study of a Manned Orbital Telescope. D2-84042-1 (Contract NAS 1-3968), Boeing Co., Oct. 1965. (Available as NASA CR-66047.)

6. Anon.: A System Study of a Manned Orbital Telescope – Synchronous Orbit Study. D2-84042-2 (Contract NAS 1-3968), Boeing Co., Apr. 1966. (Available as NASA CR-66102.)

7. Varga, John M.: Development of a Microinch Actuator. PCD-TR-68-6, FHR 3352-1 (Contract No. NAS 1-7018), Republic Aviation Div., Fairchild Hiller Corp., Mar. 24, 1968. (Available as NASA CR-66626.)

8. Rupp, Richard: Development of a Microinch Actuator. PCD-TR-69-3, FHR 3352-2 (Contract No. NAS 1-7018), Republic Aviation Div., Fairchild Hiller Corp., Apr. 28, 1969. (Available as NASA CR-66795.)

9. Crane, Robert J.: Advanced Figure Sensor. NASA CR-1659, 1970.

10. Creeden, J. F.; and Lindgren, A. C.: Control of the Optical Surface of a Thin, Deformable Primary Mirror With Application to an Orbiting Astronomical Observatory. Automatica, vol. 6, no. 5, Sept. 1970, pp. 643-660.

11. La Fiandra, Carlo: Research and Development Study of a Peristaltic Action Microinch Actuator. NASA CR-1658, 1970.

12. Robertson, Hugh J.: Evaluation of the Thin Deformable Active Optics Mirror Concept. NASA CR-2073, 1972.

13. Robertson, Hugh J.: Development of an Active Optics Concept Using a Thin Deformable Mirror. NASA CR 1593, 1970.

14. Morrell, Frederick R.: An Investigation of the Fine-Pointing Control System of a Soft-Gimbaled Orbiting Telescope. NASA TN D-5829, 1970.

15. Ostroff, Aaron J.; and Romanczyk, K. C.: Design of an Electronically Scanned Star Sensor With Digital Output. NASA TN D-5281, 1969.

16. McCarthy, Daniel J.: Operating Characteristics of the Stratoscope II Balloon-Borne Telescope. IEEE Trans. Aerosp. & Electron. Syst., vol. AES-5, no. 2, Mar. 1969, pp. 323-329.

17. Romanczyk, K. C.; Ostroff, Aaron J.; and Howell, W. E.: Design and Analysis of a Star Image Motion Compensator. NASA TN D-7145, 1973.

18. D'Azzo, John J.; and Houpis, Constantine H.: Feedback Control System Analysis and Synthesis. Second ed., McGraw-Hill Book Co., Inc., c.1966.

19. Kuo, Benjamin C.: Analysis and Synthesis of Sampled-Data Control Systems. Prentice-Hall, Inc., c.1963.

20. Bower, John L.; and Schultheiss, Peter M.: Introduction to the Design of Servomechanisms. John Wiley & Sons, Inc., c.1958.

NATIONAL AERONAUTICS AND SPACE ADMINISTRATION
WASHINGTON, D.C. 20546

OFFICIAL BUSINESS
PENALTY FOR PRIVATE USE $300

SPECIAL FOURTH-CLASS RATE BOOK

POSTAGE AND FEES PAID
NATIONAL AERONAUTICS AND SPACE ADMINISTRATION
451

U.S.MAIL

POSTMASTER: If Undeliverable (Section 158 Postal Manual) Do Not Return

"The aeronautical and space activities of the United States shall be conducted so as to contribute . . . to the expansion of human knowledge of phenomena in the atmosphere and space. The Administration shall provide for the widest practicable and appropriate dissemination of information concerning its activities and the results thereof."

—NATIONAL AERONAUTICS AND SPACE ACT OF 1958

NASA SCIENTIFIC AND TECHNICAL PUBLICATIONS

TECHNICAL REPORTS: Scientific and technical information considered important, complete, and a lasting contribution to existing knowledge.

TECHNICAL NOTES: Information less broad in scope but nevertheless of importance as a contribution to existing knowledge.

TECHNICAL MEMORANDUMS: Information receiving limited distribution because of preliminary data, security classification, or other reasons. Also includes conference proceedings with either limited or unlimited distribution.

CONTRACTOR REPORTS: Scientific and technical information generated under a NASA contract or grant and considered an important contribution to existing knowledge.

TECHNICAL TRANSLATIONS: Information published in a foreign language considered to merit NASA distribution in English.

SPECIAL PUBLICATIONS: Information derived from or of value to NASA activities. Publications include final reports of major projects, monographs, data compilations, handbooks, sourcebooks, and special bibliographies.

TECHNOLOGY UTILIZATION PUBLICATIONS: Information on technology used by NASA that may be of particular interest in commercial and other non-aerospace applications. Publications include Tech Briefs, Technology Utilization Reports and Technology Surveys.

Details on the availability of these publications may be obtained from:

SCIENTIFIC AND TECHNICAL INFORMATION OFFICE

NATIONAL AERONAUTICS AND SPACE ADMINISTRATION

Washington, D.C. 20546